Modulation of riverine concentration-discharge relationships by changes in the shape of the water transit time distribution

Mark A. Torres[1], **J. Jotautas Baronas** [2]

[1]Department of Earth, Environmental, & Planetary Sciences, Rice University
[2]Department of Earth Sciences, University of Cambridge

Key Points:

- Model coupling hydrology with mineral dissolution/precipitation kinetics to predict concentration-discharge relationships for cations and Si
- Changes in concentrations and ratios with discharge affected by coincident changes in the shape of transit time distribution
- Model captures the majority of field concentration-discharge relationships, including positive relationships, but reveals equifinality

Corresponding author: Mark A. Torres, `mt61@rice.edu`

Abstract

The concentrations of weathering-derived solutes in rivers and their co-variance with discharge are thought to reflect reactive-transport processes in hillslopes and to reveal the sensitivity of solute fluxes to climatic change. It is expected that discharge-driven changes in water transit times play some role in setting concentration-discharge (C-Q) relationships, but knowledge gaps remain. To explore the specific role of changes in the shape of the transit time distribution with discharge, we combine models to simulate C-Q relationships for major cations and Si as example solutes with contrasting affinities to partition into secondary phases. The model results are compared with an analysis of C-Q relationships using the Global River Chemistry Database.

We find that changes in the shape of the transit time distribution with discharge can produce a range of cation-Q and Si-Q relationships that encompasses most of the range observed in real catchments, including positive Si-Q relationships and variable cation to Si ratios. We find that C-Q relationships (characterized by power law exponents) can remain approximately constant, even as the Damköhler Number (ratio of transport timescale to reaction timescale) is varied over three orders of magnitude. So, in our model analysis, C-Q relationships are as sensitive to hydrologic variability as they are to reaction rates. Additionally we find that, depending on the storage-discharge relationship, changes in rainfall patterns can influence C-Q relationships. Altogether, our results suggest ways in which C-Q relationships may be non-stationary in response to climatic change and/or vary in space and time due to catchment hydrologic properties.

1 Introduction

The chemical reactions between water, atmospheric gases, and minerals occurring in terrestrial systems play an important role in global biogeochemical cycles. The major dissolved products of these weathering reactions (Na, K, Ca, Mg and Si) are ultimately transported to the ocean by rivers. As such, much research has focused on the chemical composition of river waters as a means to quantify net weathering fluxes and infer the environmental parameters controlling them (Meybeck, 1987; Gaillardet et al., 1999; Godsey et al., 2019). Of particular interest is how the fluxes of cations derived from the dissolution of silicate minerals respond to changes in temperature and/or rainfall since this behavior may constitute a negative feedback that regulates atmospheric CO_2 levels and, by extension, global climate (Ebelmen, 1845; Walker et al., 1981).

The flux of a weathering-derived solute carried by a river is equal to the product of the measured flow rate (discharge) and the measured solute concentration. Characterizing the degree to which these quantities co-vary is important for accurately quantifying fluxes (Stelzer & Likens, 2006) and may also hold information about the underlying hydrochemical processes (Anderson et al., 1997; Godsey et al., 2009; Clow & Mast, 2010; Maher, 2011; Herndon et al., 2015; Torres et al., 2015; Winnick et al., 2017; Wymore et al., 2017; Hunsaker & Johnson, 2017; Hoagland et al., 2017; Diamond & Cohen, 2018; Herndon et al., 2018; Samanta et al., 2019; Knapp et al., 2020). For example, these so-called concentration-discharge (C-Q) relationships may reflect changes in the path and/or rate of water flow through the landscape, affecting the availability of different mineral surfaces for reaction and/or the total amount of time over which reactions can occur. However, distinct processes can often lead to similar C-Q behavior and these processes need not be mutually exclusive. Moreover, the aggregation of heterogeneous sub-catchments (Torres, Baronas, et al., 2017; Bouchez et al., 2017) as well as reactions occurring within the stream channel itself (Baronas et al., 2017; Guinoiseau et al., 2016) and/or at the groundwater-surface water interface (Kim et al., 2017) may also contribute to C-Q behavior. This equifinality represents a major complication as, without knowing the exact mechanisms responsible for setting C-Q behavior, it is difficult to predict how weathering fluxes will vary in response to Earth system change.

The *null* hypothesis for C-Q relationships is that solute concentrations will vary inversely with discharge, referred to as dilution behavior. This behavior can arise from changes in either source mixing or reaction progress as a function of discharge. For example, if weathering systems behaved as simple mixed-flow or plug-flow reactors with constant reaction kinetics, then concentrations should vary with discharge following an inverse relationship:

$$C = kVQ^{-1} \tag{1}$$

where V is the fluid volume of the system, Q is a volumetric fluid flow rate, and k is a constant of proportionality relating transit time with solute concentration. This simple dilution relationship (i.e., $\mathrm{C} \propto \mathrm{Q}^{-1}$) fails to describe the majority of river systems that have been investigated (Godsey et al., 2009). Instead, the concentrations of weathering-derived solutes tend to vary much less than water discharge (e.g., a factor of 10 increase in Q may drive a decrease in C that is less than a factor of 2; Godsey et al., 2009). Termed "chemostasis", this type of concentration-discharge (C-Q) behavior implies that solute fluxes increase with increasing discharge, with important implications for the nature and sensitivity of weathering-climate feedbacks (Gaillardet et al., 2011; Maher & Chamberlain, 2014).

Typically, the degree to which a catchment behaves chemostatically is quantified by fitting the C-Q relationship with a power law model:

$$C = a \cdot Q^{b} \tag{2}$$

where a is a pre-factor and b is an exponent. Due to spurious correlation between the values of a and b, it can be difficult to interpret the fitted value of the pre-factor a (Dralle et al., 2015; Knapp et al., 2020). Instead, the value of the exponent b is a useful metric to distinguish between chemostatic behavior ($b = 0$) and simple dilution (b = -1; Godsey et al., 2009).

Idealized models attempting to explain the origin of chemostasis usually focus on either water-table driven changes in reactive surface area (Godsey et al., 2009), thermodynamic limits on solute concentrations and reaction rates (Maher, 2011; Maher & Chamberlain, 2014; Ameli et al., 2017), or both (Eiriksdottir et al., 2013). In essence, these models deviate from Equation 1 in that they introduce variability in the reaction rate term (k) that compensates for the predicted dilution with increasing Q (Equation 1). Fundamentally, these (and similar) models all treat C-Q relationships as a reactive transport phenomenon, but differ slightly in the exact functional form of the resulting C-Q relationship.

In principle, comparing the different predictions of existing C-Q models to field data could be used to infer the dominant mechanisms driving C-Q behavior in natural systems. However, scatter in the data and non-uniqueness complicate distinguishing mechanisms based on model-data comparisons (Chanat et al., 2002; Godsey et al., 2009; Wymore et al., 2017; Ibarra et al., 2017). At the same time, existing model formulations make limiting assumptions that may not be applicable to all natural systems. For example, the model of Godsey et al. (2009) assumes that weathering reactions occur far-from-equilibrium despite field observations of near-equilibrium weathering (Maher et al., 2009; Ibarra et al., 2016) and elemental and isotopic ratio data from rivers consistent with substantial secondary silicate mineral formation (Georg et al., 2007; Cardinal et al., 2010; Frings et al., 2015).

The effects of near-equilibrium conditions and associated secondary mineral formation *are* included in the C-Q model of Maher and Chamberlain (2014). However, this model assumes that the water transit time distribution (TTD) has a fixed exponential shape, which is in contrast to evidence for time-variable TTD shapes (Benettin, Kirchner, et al., 2015; Kaandorp et al., 2018; Onderka & Chudoba, 2018; Knapp et al., 2019;

Wilusz et al., 2020). While the near-equilibrium or TTD shape assumptions are not *essential* components of either the Godsey et al. (2009) or the Maher and Chamberlain (2014) models, respectively, their presence in published formulations may mean that the parameter values calculated through inverting field data include an unknown amount of error complicating catchment-to-catchment comparisons (Ibarra et al., 2017; Wymore et al., 2017). Moreover, model structure may play an important role when implementing C-Q theory into Earth System models due to specific assumptions for how C-Q relationships change in response to climatic forcing (Von Blanckenburg et al., 2015; Ibarra et al., 2016).

Other conceptual models for C-Q behavior exist including some that attribute it to end-member mixing (e.g., Johnson et al., 1969; Christophersen et al., 1990; Neal et al., 1990; Chanat et al., 2002; Calmels et al., 2011). The generation of multiple water masses with distinct chemical compositions could arise from spatial differences in the composition of solid-phases (e.g., different compositions for surface soils versus deeper bedrock) and would help explain patterns in hydrochemcial datasets that appear to be consistent with conservative mixing (Christophersen et al., 1990; Calmels et al., 2011; Lee et al., 2017; Baronas et al., 2020). Similarly, differences in C-Q behavior for different elements in the same system (i.e., variations in elemental ratios with discharge) are sometimes attributed to variations in the solid-phase composition between and along flow paths (Kurtz et al., 2011; Calmels et al., 2011; Torres et al., 2015; Winnick et al., 2017; Zhi et al., 2019).

Given the carbon cycle significance of silicate weathering in particular, it is of interest to build C-Q models the focus solely on solutes derived from this process (e.g., Eiriksdottir et al., 2013; Maher & Chamberlain, 2014) and, in field data, correct measured solute concentrations so that they reflect only the proportion that is derived from silicate weathering. Of the major elements, both Na and Si require only a few assumptions to determine their silicate weathering-derived concentrations in most rivers (Gaillardet et al., 1999). As a result, these elements in particular are useful tracers for comparing model results with field data for assessing silicate C-Q relationships.

In global compilations, there is a tendency for Na concentrations to decrease more with increasing discharge relative to Si concentrations at individual sites (i.e., Si is more chemostatic than Na; Godsey et al., 2019). This divergent C-Q behavior of Na and Si typically leads to decreases in the dissolved Na to Si ratio with increasing discharge (Torres et al., 2015). Additionally, Si variations are characterized by a positive C-Q relationship at many sites (i.e. concentrations increase with increasing discharge; Aguirre et al., 2017; Godsey et al., 2019), which is unlike most other weathering-derived solutes and not predicted by any reactive-transport model of C-Q behavior. These differences between Na and Si are notable as both elements are sourced from some of the same silicate mineral phases (e.g., albite; $NaAlSi_3O_8$) such that solid-phase compositional heterogeneity may not always be a viable mechanism to explain their contrasting C-Q behavior.

Given their shared primary source, the origin of Na/Si fractionation may instead relate to the secondary formation of cation-poor silica phases (e.g., biogenic opal and phyllosilicates) that act to buffer dissolved Si concentrations decoupling their behavior from other silicate-derived solutes like Na. The formation of such phases is consistent with the Si isotopic composition of river waters, which is fractionated relative to primary silicate minerals (Georg et al., 2007; Cardinal et al., 2010; Frings et al., 2015). Furthermore, co-variation between Si isotopic ratios and the ratio of dissolved Ge to Si implies that phyllosilicate phases are a more common control on Si behavior as opposed to biogenic opal (Baronas et al., 2018), though exceptions exist (Derry et al., 2005). While some existing C-Q models explicitly include the formation of secondary silicate phases (e.g., Maher, 2011; Maher & Chamberlain, 2014), they do not leverage Na/Si fractionation as a constraint on model parameters and, as stated previously, are incapable of generating the positive Si-Q relationships seen in many river systems. As such, it remains unclear if changes in elemental ratios with discharge and/or positive Si-Q relationships are con-

sistent with current reactive-transport theories for C-Q dynamics or if they always require additional processes such as solid-phase heterogeneity or the formation and transport of colloidal Si (Trostle et al., 2016; Aguirre et al., 2017).

In this contribution, we utilize a simple numerical model to explore the C-Q behavior of cations and Si in an idealized catchment system and compare the results to a global compilation of riverine C-Q relationships. To determine how sensitive C-Q dynamics are to variations in catchment hydrology, we use the modeling approach of Kirchner (2016b), which allows transit time distributions to vary in shape with discharge. Our aim is to test how much variability in C-Q can be generated without invoking variation in the solid-phase composition between and along water flow paths. To do this, we assume a homogeneous distribution of reactive primary minerals, such as that expected in steep, erosion-dominated catchments, and generate chemostasis through a coupled kinetic-thermodynamic reaction framework (following Maher, 2011). While this assumption of solid-phase homogeneity may not apply to all watersheds, it represents a useful reference case to assess the potential role of hydrologic variability in setting C-Q relationships for silicate weathering processes.

2 Methods

2.1 Numerical Model

2.1.1 Equations for calculating water fluxes

Natural hydrologic systems are dynamic due to time-varying inputs (rainfall) and changes in internal storage that influence the output signal (river flow) in terms of its magnitude and age (Harman, 2015; Benettin, Kirchner, et al., 2015; Knapp et al., 2019). Following Kirchner (2016b), a simple way to simulate such non-stationary behavior is using a two-box hydrologic model with "upper" and "lower" boxes. Hereafter in the manuscript, this model will be referred to as the 2-box Kirchner (2BK) Model.

Rainfall inputs (P) into the upper box fill the upper storage reservoir (S_U), which is drained into both the lower box and directly to river discharge (Q). The proportion of the total upper box outflow (O_U) that is partitioned into discharge is fixed at a value η. The proportion of upper box outflow that enters the lower box (i.e., 1-η) fills the lower storage reservoir (S_L), which drains solely to discharge. For both boxes, storage is calculated by mass balance (i.e., inputs minus outputs). The output flux from each box is assumed to be proportional to the total storage within the box (via the constant of proportionality κ) raised to some power β. Given this model structure, the change in storage over time in each box is calculated as:

$$\frac{dS_U}{dt} = P - \kappa_U S_U^{\beta_U} \tag{3}$$

and

$$\frac{dS_L}{dt} = \left((1-\eta)(\kappa_U S_U^{\beta_U})\right) - \kappa_L S_L^{\beta_L} \tag{4}$$

As such, the 2BK model only accounts for sub-surface storage dynamics and neglects all effects of near-surface evapo-transpiration on the flux, age, and chemical composition of surface waters.

Simulations using Equations 3 and 4 were conducted using the numerical solution presented in Kirchner (2016b), which is a weighted combination of the trapezoidal and backwards Euler methods with a fixed daily time-step, and the `fsolve` function in MATLAB2020a with default options. In addition to computing river discharge, we use the

method described in Kirchner (2016b) to calculate the concentration of a conservative tracer in the river outflow at each time-step given a time-varying input concentration. The purpose of this calculation is to get a rough assessment of the storage duration before the Monte-Carlo determination of age distributions is done (see below).

We model the conservative tracer input as a sine wave with the same period (1 year) and phase (peak on Dec. 27th) for all of the simulations. In natural systems, the concentration or ratio value of conservative tracers like Cl, ^{18}O/^{16}O, and D/H can be positively correlated (Kirchner et al., 2000; Bowen, 2008), negatively correlated (Bowen, 2008), or un-correlated with rainfall amounts. In other words, in different catchments, the phasing of the conservative tracer cycle varies relative to the cycle of precipitation amount. In a set of preliminary experiments, we found that varying the phase offset between the conservative tracer and precipitation amount cycles would, under some conditions, have a large impact on the amplitude of the conservative tracer variations in the modeled outflow. However, we decided that further investigation of this effect is beyond the scope of this study and instead used an identical phasing as in previous model iterations (Kirchner, 2016b).

2.1.2 Method for extracting conditional transit time distributions

To extract the full transit time distribution from non-steady simulations with the 2BK model, we utilized a Monte-Carlo approach that is similar to the methods described in McMillan et al. (2012) and Klaus et al. (2015). This approach involves discretization whereby we track the age of a large number of water parcels that enter and exit storage at rates I^* and O^*, which are proportional to the calculated input and output fluxes of water for each box, respectively. To ameliorate truncation errors, the flux of water parcels is set equal to 1000 times the water flux (i.e., we preserve three decimal places of precision in the water input and output — rainfall and discharge — values).

At each time step, we fill I^* random empty cells ($I^* = 1000{\cdot}P$) of a matrix representing the upper storage box with zeros (representing water parcels with zero ages) and extract O_U^* values ($O_U^* = 1000{\cdot}O_U$) from random filled positions and replace them with NaN values (representing empty space). A fraction (equal to 1-η) of the values extracted from the upper box are selected at random and added to the matrix representing the lower storage box. The remainder of the values extracted from the upper storage box enter discharge. Additionally, O_L^* values ($O_L^* = 1000{\cdot}O_L$) from random filled positions are removed from the matrix representing the lower storage box and added to discharge. At the end of each time-step, cells not filled with NaN values in either storage matrix have their value increased by one (i.e., water parcels remaining in storage are aged by one day). At any given time-step, the water transit time distribution is then represented by age distributions of the discharged water parcels.

The results of the Monte-Carlo analysis produce daily estimates of transit time distributions in the form of ages for a number of water parcels exiting storage at each time-step. To focus on the average behavior of the model, the daily TTDs were grouped together based on their associated discharge values. Specifically, we partitioned the data by discharge into 10 bins with each bin representing 10% of the full distribution of river discharge (deciles). So, for example, the water parcel ages for all days where discharge was within the range defined by 10th and 20th percentiles of the full discharge distribution were grouped together and used to calculate a single TTD. This single TTD was then assigned to represent a discharge equal to the mean of the associated discharge decile.

With this approach, each discharge bin contains an approximately equal number of days, but, as the total volume of water in transit varies with discharge, each bin contains a different number of water parcels. Accordingly, we generated an empirical cumulative distribution function from the water parcel ages within each discharge bin (MATLAB2020a function `ecdf`) and, using inverse transform sampling, generated an equal num-

ber of random draws from each conditional transit time distribution to be used in Si and cation concentration modeling as described below. Prior to these calculations, we normalized the transit time values by the discharge-weighted mean transit time (μ_Q) for the individual simulation. We symbolize this dimensionless transit time using the variable τ^* in order to distinguish it from dimensionless weathering time (t^*), which we introduce below.

2.1.3 Equations for calculating weathering-derived solute concentrations

Silicate weathering involves both dissolution and precipitation reactions with the net solute release to rivers reflecting the balance between the two. The extent to which different elements are taken up into secondary precipitates is variable and, for some elements, is poorly constrained (Moulton et al., 2000; Bickle et al., 2015; Frings et al., 2016). However, it is typically assumed that high proportions of major cations remain in solution instead of being incorporated into secondary phases (Gaillardet et al., 1999). In contrast, a significant proportion of the total Si release is expected to be removed from solution via the formation of secondary silicate phases (Frings et al., 2016; Baronas et al., 2018). Accordingly, it is reasonable to model cation release solely as a dissolution reaction whereas, for Si, it is necessary to account for the effects of both dissolution and precipitation on solute concentrations.

The rates for both dissolution and precipitation reactions depend on a range of parameters including solution composition, temperature, and reactive surface area (Brantley et al., 2008; Schott et al., 2009). In addition, net reaction rates must slow to zero as fluids approach thermodynamic equilibrium and increase towards the kinetic limit with increasing distance from equilibrium (Brantley et al., 2008; Schott et al., 2009). The purpose of our study is to isolate and examine the particular role of weathering reaction timescales on the final discharged fluid composition. For this reason, we assume that dissolution rates vary only as a function of solution composition, that dissolution rates decrease with increasing reaction progress, and that reactions have an end point where net rates go to zero.

These assumptions are implemented for dissolution (d) reactions as

$$\frac{d[C]}{dt} = R_d \cdot \left(1 - \frac{[C]}{[C]_{eq,d}}\right)^{m,d} \tag{5}$$

where $[C]$ is the concentration of a solute (μM), R_d is the product of a dissolution rate constant and a constant reactive surface area and, here, is equal to the maximum possible solute release rate (μM day^{-1}), $[C]_{eq}$ is the solute concentration where net reaction rates go to zero (μM), and m, d is an exponent that affects how rates slow with reaction progress.

Our assumption of a negative relationship between dissolution rates with reaction progress can be thought of as a thermodynamic limit (*sensu* Maher & Chamberlain, 2014) or, more generally, a negative feedback on reaction rates. Separate from a thermodynamic control, experimental data show that reaction rates for some silicate minerals decrease with increasing pH up to pH values of about 8. A negative pH dependence could lead to a decrease in reaction rates with increasing reaction progress as the alkalinity generated from silicate weathering acts to increase solution pH assuming all other factors are held constant. Other reaction products also act to slow dissolution rates at far-from-equilibrium conditions such as the inhibition of feldspar and other aluminosilicate mineral dissolution by dissolved Al (Schott et al., 2009; Eiriksdottir et al., 2013). Additionally, from a purely empirical stand-point, field measurements of mineral dissolution rates are negatively correlated with the duration of water/rock interaction (Maher, 2010; Reeves & Rothman, 2013), which is re-produced by Equation 5.

To model precipitation reactions, precipitation rates are assumed to be zero until a threshold concentration is reached at which point rates increase with increasing reactant concentrations. This is modeled with the equation:

$$\frac{d[C]}{dt} = R_p \cdot \mathbf{H}\Big(\frac{[C]}{[C]_{eq,p}} - 1\Big) \cdot \Big(\frac{[C]}{[C]_{eq,p}} - 1\Big)^{m,p} \tag{6}$$

where $\mathbf{H}()$ is the Heaviside function, which is added to ensure that precipitation rates are zero when the solution is under-saturated with respect to the dissolving phase (i.e., $\mathbf{H}(x) = 0$ while $C/C_{eq,p} < 1$ and $\mathbf{H}(x) = 1$ while $C/C_{eq,p} > 1$).

We model the time rate of change of cation concentrations using only Equation 5, whereas for Si, we model the time rate of change as the difference between Equations 5 and 6. We consider the dissolution of a single mineral phase, so the dissolution terms for both solutes are set proportional to each other by a value χ (mols cation /mols Si) that represents the stoichiometry of the dissolving primary mineral. To simplify the equations, we normalize cation (C_+) and Si concentrations by the concentrations where net reaction rates are equal to zero and time by the time required to reach equilibrium (T_{eq}) at the maximum dissolution rate (R_d), which yields:

$$C_+^* = \frac{[C_+]}{[C_+]_{eq,d}} \tag{7}$$

$$Si^* = \frac{[Si]}{[Si]_{eq,p}} \tag{8}$$

$$t^* = \frac{t \cdot \chi R_d}{[C_+]_{eq,d}} = \frac{t}{T_{eq}} \tag{9}$$

Substituting these definitions into Equations 5 and 6 yields:

$$\frac{dC_+^*}{dt^*} = (1 - C_+^*)^{m,d} \tag{10}$$

and

$$\frac{dSi^*}{dt^*} = \Big(\frac{[C_+]_{eq,d}}{\chi[Si]_{eq,p}}(1 - C_+^*)^{m,d}\Big) - \frac{R_p[C_+]_{eq,d}}{R_d\chi[Si]_{eq,p}}\Big(\mathbf{H}(Si^* - 1) \cdot (Si^* - 1)^{m,p}\Big)\Big) \tag{11}$$

Equation 10 has an analytical solution

$$C_+^*(t^*) = \sqrt[1-m,d]{(1 - m, d)(C_1 - t^*)} \tag{12}$$

where C_1 is a constant of integration that can be calculated from the boundary condition that $C_+^* = 0$ when $t^* = 0$. To solve Equation 11, we use numerical integration with the MATLAB2020a solver `ode45`. For each parameter set (see below), Equation 11 is integrated until Si^* is less than or equal to 1.01 (i.e., until dissolved Si is approximately equal to its equilibrium concentration). The solution of Eqs. 10 and 11 represents the evolution of cation and Si concentrations in a certain parcel of water with time along a single flowpath (i.e., one water parcel in the Monte-Carlo model).

Our choice to use non-linear reaction rate terms in Equations 10 and 11 (i.e., $m, d \geq 1$; see below) has important implications for our model as it means that the average rate of reaction within the watershed does not solely depend on the mean solute concentration within the hillslope aquifer and instead is also sensitive to the distribution of solute concentrations about this mean. As typical box model approaches assume that water storage within the catchment is well-mixed, they return only the mean solute concentration within the reservoir and thus can over-predict reaction rates (Bolton et al., 2006) and generate C-Q response with strong hysteresis patterns that are not typical of real C-Q data (Godsey et al., 2009).

To avoid the assumption of well-mixed solute concentrations, we instead take the binned transit time distributions (i.e., the relative frequency of different ages) and transform them into a distribution of concentrations using the integrated forms of Eqs. 10 and 11, which uniquely map cation and Si concentrations to water age for a single isolated flow path. This, in effect, assumes that the discharge response in the catchment behaves in a well-mixed fashion (e.g., due to a pressure wave through the hillslope aquifer), but that the fluids themselves are not physically mixed. While also an abstraction of reality (i.e., there is *some* subsurface mixing), our approach represents a useful end-member condition (isolated flowpaths) that is a more realistic representation of hillslope-scale hydrology than the well-mixed assumption, yet much easier to solve than full 3-D reactive transport simulations (e.g., Li et al., 2017).

Our general approach of transforming a predicted transit time distribution with a non-linear reaction equation is similar to that of Maher (2011), Maher and Chamberlain (2014), and Benettin, Bailey, et al. (2015). The differences between those models and the work here is that we use the 2BK hydrologic model to generate non-stationary transit time distributions with a wide range of shapes more similar to those expected for natural systems (Kirchner et al., 2000; Godsey et al., 2010; Kirchner, 2016b; Benettin, Kirchner, et al., 2015; Knapp et al., 2019; Wilusz et al., 2020). In the work of Maher and Chamberlain (2014), they strictly assumed that, for a given value of discharge, transit times were exponentially distributed and that the mean transit time varied inversely with discharge. While Maher (2011) simulated a wider range of gamma-distributed TTD shapes, this work still assumed that TTD shapes were constant and did not vary with discharge. Our reaction model treats dissolution and precipitation separately whereas the reaction models of Maher (2011), Maher and Chamberlain (2014), and Benettin, Bailey, et al. (2015) lumped these two reactions together and modeled only the *net* release of solutes. These differences, as well as our broad parameter search (see below), allow for a wider range of model behavior than considered in previous studies. In particular, we are able to explore the contrasting effect that changing TTD shape has on the concentrations of cations and Si, which are expected to differ in their degree of incorporation into secondary phases.

2.1.4 Parameter choices for computing water fluxes and ages

The 2BK model requires an input rainfall time-series as well as five parameter values (Eqs. 3-4). As many of these parameters cannot be directly measured in natural systems, we use random parameter sampling to determine the range of possible model behaviors and then focus our analysis on a subset of the model simulations representing this range.

Three different natural rainfall time-series are used to drive three iterations of the 2BK model. Specifically, we select rainfall time-series from the Broad River (GA, USA) and Smith River (CA,USA) catchments following Kirchner (2016b). We also use data from the Bisley catchment in Puerto Rico (Ruiz, 2019) in lieu of the Plynlimon catchment (Wales, U.K.) used by Kirchner (2016b) in order to include an even higher rainfall rate input forcing ($\sim$9 vs. $\sim$7 mm/day average rainfall rates for Bisley vs. Plynlimon). In addition to different rainfall rates, the three input time-series also differ in their temporal patterns. Specifically, the Smith River forcing has a high amplitude seasonal cycle that is not present in the other two input time-series. Fifteen years of rainfall data were used for each simulation where the first five years were used as a spin-up period for the model to achieve a long-term balance between water input (rainfall) and output (discharge). For the Broad and Smith River inputs, we used 15 continuous years of data. For the Bisley input time-series, we replicated one year during the spin-up period and had one instance of two non-consecutive years being run as consecutive.

For each rainfall time-series, the model was run 5000 times, each time randomly drawing the hydrologic parameter values from specified distributions (Table 1). Follow-

ing Kirchner (2016b), we do not randomly draw κ values directly and instead draw "reference" storage values for each box (S_U^* and S_L^*) that are equal to:

$$S_U^* = \left(\frac{\kappa_U}{\bar{P}}\right)^{\frac{1}{-\beta_U}} \tag{13}$$

$$S_L^* = \left(\frac{\kappa_L}{(1-\eta)\bar{P}}\right)^{\frac{1}{-\beta_L}} \tag{14}$$

where $\bar{P}$ is the average rainfall input. These reference storage values represent the expected storage volume for long-term input/output balance and, as parameter values, are more manageable to sample than κ due to the co-variability between κ and β values. The parameter ranges we selected are identical to Kirchner (2016b) except for η, which we allow to have a wider range (0.01 to 0.9). The exact ranges and distributions for all 2BK model parameter sampling are provided in Table 1.

Using the output discharge and conservative tracer time-series from last 10 years of each model simulation, we cluster the model results using k-means clustering to identify distinct model behaviors for each of the three input time-series. For a given rainfall input time-series, the clusters encapsulate the range of behaviors observed in the full (5000-run) Monte Carlo simulation set. We use this clustering approach to reduce the processing time required for the more computationally expensive extraction of a full transit time distribution at each model time-step as well as for interpretive simplicity (i.e., we focus on a smaller number of representative model simulations that can be interrogated in more detail than the full 5000 member ensemble).

To perform the k-means clustering, we first normalized the discharge and tracer concentration time-series by the mean and standard deviation from the entire 5000 member ensemble generated from a single input time-series using the MATLAB2020a function `zscore`. The purpose of this transformation was to give nearly equal weight to both discharge and tracer concentrations while also preserving differences in the absolute values between ensemble members that would be lost if each was normalized by its own mean and standard deviation. Using the normalized data, we computed the average normalized discharge and tracer concentration for each day of the year using the last 10 years of model output from each parameter combination. The data were averaged in this way in order to limit the influence of inter-annual variability in rainfall on the cluster selection. Finally, we used the MATLAB2020a function `kmeans` to cluster the model results based on 732 descriptors for each parameter combination (i.e., a annual cycles of average daily discharge and tracer concentrations including 3 to 4 leap years depending upon the input time-series).

Initially, we tested a range from 2 to 40 clusters and computed the sum of squared deviations between the time-series associated with the cluster centroids and each model simulation. By visually inspecting the relationship between within cluster differences and the number of clusters, we identified 10 clusters as being a reasonable parameter choice to generate well-defined clusters while not over-fitting the data. To select a combination of model input parameters (i.e., S_U^*, β_U, *etc.*) to represent each cluster, we selected the model simulation within each cluster that had the smallest sum of squared differences from the cluster centroid and saved the parameters associated with this simulation. In total, we generated a set of 30 parameters combinations to be used to represent the range of behaviors produced by the 2BK model (i.e., ten for each rainfall input time-series).

The parameter combinations identified by clustering the model results from any given rainfall input time-series do not exactly match the parameter combinations identified from the simulations using the other rainfall inputs and *vice versa*. Accordingly, we took the 30 parameter sets we identified and used them to simulate discharge with all three input time-series before applying our Monte-Carlo approach to determining tran-

sit time distributions (Section 2.1.2). Altogether, this approach yielded a total of 90 hydrologic model simulations with conditional TTDs for our analysis. The exact 2BK model parameter sets utilized in this study are provided in Table S1.

2.1.5 Parameter choices for computing solute concentrations

For two weathering-derived solutes (a cation and Si), four dimensionless parameters are required to model their concentration versus time relationships (Eqs. 10-11). As such, a similar clustering approach was applied to the weathering model after performing 10^3 simulations with random parameter values selected from set distributions (ranges and distribution shapes in Table 2). The parameter ranges were selected to be broadly consistent with weathering systems, but still produce a wide range of model behaviors.

For the dissolution and precipitation rate exponents (m, d and m, p), the range from 1 to 2 is consistent with non-linear changes in reaction rates observed in laboratory experiments (Taylor et al., 2000; Hellmann & Tisserand, 2006; Daval et al., 2010) and field data (Maher et al., 2009; Maher, 2011; Reeves & Rothman, 2013) as well as expected from theory (Shiraki & Brantley, 1995; Dove et al., 2005). For the normalized ratio of equilibrium concentrations, we expect that $[Si]_{eq}$ will be similar to or lower than "equilibrium" cation concentrations ($[C_+]_{eq}$) and that the molar ratio of cations to Si in the dissolving mineral phase (χ) will be less than or equal to 1/2 (feldspar stoichiometry), which, together, should lead to values greater than 1 for this parameter. For the ratio of the baseline precipitation rate to the maximum dissolution rate (R_p/R_d), we selected a large range in order to allow for a variable degree of super-saturation with respect to secondary mineral phases — as is observed in natural systems (Ibarra et al., 2016) — while also remaining consistent with laboratory rate measurements (Zhu et al., 2010, 2016). In general, it is expected that secondary mineral precipitation rates are slow relative to primary mineral dissolution rates (Maher et al., 2009; Zhu et al., 2010). However, in order to have Si not exceed its equilibrium concentration, as is specified in some existing models (Maher, 2011), it may be necessary to have relatively rapid rates of secondary mineral precipitation at low degrees of super-saturation, which is re-produced by our parameter ranges. Since our definitions of both R_p and R_d incorporate both an intrinsic rate constant and a constant reactive surface area, they are not directly comparable to laboratory determinations of rate constants, which are typically surface area normalized.

Since our solution scheme for Equation 11 leads to variable time steps for each model run, we fit the results by linear interpolation to re-sample concentrations at consistent time intervals. The model behavior for both C_+^* and Si^* was evaluated over a range of t^* from 0 to 11 and used as the inputs to the MATLAB2020a function `kmeans`. The same approaches to selecting the optimal number of clusters ($n = 20$) and finding a representative parameter set for each cluster that are described in Section 2.1.4 were also utilized for clustering the results of the weathering model. The exact weathering model parameters utilized in this study are provided in Table S2.

2.1.6 Combining the hydrologic and weathering models

The conditional age distributions generated using the hydrologic model are all normalized by the discharge-weighted mean transit time (μ_Q) for a given simulation, yielding a dimensionless transit time that we denote as τ^*. In contrast, the output from the weathering model is normalized by the equilibrium timescale yielding a dimensionless weathering time that we denote as t^*. When evaluated at the same absolute value of time (t; days), the ratio of the normalized weathering time to the normalized transit time is a Damköhler number:

$$\frac{t^*}{\tau^*} = \frac{\frac{t}{Teq}}{\frac{t}{\mu_Q}} = \frac{\mu_Q}{Teq} = \mathrm{Da} \tag{15}$$

Here, we specify Da to be 0.1, 1, 10, or 100 and then re-scale the dimensionless transit time distribution accordingly, yielding a set of 3,600 re-scaled TTDs (90 sets of 10 TTDs binned by discharge, re-scaled at four different Da values each). Using a given set of kinetic model parameters, we then calculated the mean C_+^* and Si^* concentrations for each TTD. This was done by evaluating the solute release functions (Eqs. 10 and 11) at $1{\cdot}10^6$ random values drawn from each re-scaled TTD and taking the mean, yielding a total of 3,600 simulated C_+^* and Si^* concentrations each (distributed over 10 discharge bins of 360 model runs). We then fit the C-Q relationships for each model to a power law relationship (Equation 2) using the MATLAB2020a Curve Fitting Toolbox with default options, yielding 360 C_+^*-Q and Si^*-Q relationships each. This procedure was then repeated for each of the 20 sets of selected kinetic model parameters, yielding a total of 7,200 simulated C_+^*-Q and 7,200 simulated Si^*-Q relationships.

Normalizing fluid transit time by the discharge-weighted mean transit time is potentially problematic for heavy-tailed age distributions, as slight variations in the oldest age can significantly affect the mean. This could introduce variability between each of the dimensionless age distributions that is mostly due to extreme values from the Monte-Carlo analysis as opposed to the overall distribution shape. Since the normalization by the discharge-weighted mean transit time also appears in Equation 15, the potential consequence of variability resulting from extreme values would be an incorrect interpretation that the dynamics of the hydrologic model influence C-Q behavior at a fixed value of Da. To test whether or not normalizing by the mean affects our interpretations, we also normalized the transit time distributions by the discharge-weighted median transit time, as well as the discharge-weighted trimmed mean transit time (i.e., the mean after removing data below the 25th percentile and above the 75th percentile), and incorporated these alternative normalizations in the definition of the Damköhler number (i.e., replaced the mean transit time with the median or trimmed-mean transit time in Equation 15). The full sequence of modeling steps is summarized in Figure 1.

2.2 Data Compilation

2.2.1 GloRiCh

To characterize global C-Q relationships, we utilized the Global River Chemistry (GloRiCh) database of Hartmann et al. (2014). As with previous global C-Q analyses (Moon et al., 2014; Ibarra et al., 2017), this database includes data from the United States Geological Survey, HyBAm, and GEMS. In addition to these sources, GloRiCh also includes data from other governmental monitoring programs and the scientific literature (see reference list in Torres, Moosdorf, et al., 2017). A C-Q analysis using the GloRiCh database was most recently performed by Godsey et al. (2019), though here we utilize a slightly different set of quality control and data wrangling procedures.

For quality control, we excluded individual analyses where reported discharge values are less than or equal to zero. To focus on silicate-derived solutes, we restricted our C-Q analysis to dissolved Na and Si. No correction to the Si data was applied. For Na, rainwater contributions were subtracted from the total as:

$$[Na]_{sil} = [Na]_{riv} - ([Cl]_{riv} \cdot 0.857) \tag{16}$$

where brackets denote concentrations, the subscript *sil* denotes the concentration of an element derived from silicate dissolution, and the subscript *riv* refers to the total concentration of a solute measured in a river water sample. The value of 0.857 is the Na to

Cl ratio of seawater. This approximation of the rainwater Na to Cl ratio as being equal to the seawater Na to Cl ratio is not altogether unreasonable as seawater is typically the major source of these ions to rain waters (Vet et al., 2014) and, even at inland sites, rainwater Na to Cl ratios are measured to be close to the seawater ratio (Stallard & Edmond, 1981). Moreover, when different from seawater, rainwater Na to Cl ratios appear to vary within a relatively narrow range (0.5 to 1.6; Möller, 1990) relative to other elemental ratios such as SO_4/Cl, which can be over an order of magnitude higher in rainwater compared to seawater (Torres et al., 2018). If, for an individual sample, this correction returned a negative value for $[Na]_{sil}$, this sample was removed from consideration. We note that this rainwater correction was not conducted in Godsey et al. (2019).

The chloride correction (Equation 16) is imperfect as it does not explicitly account for Cl inputs from evaporite mineral dissolution, road salts, and/or hot spring discharge. Since each of these additional solute sources is likely to have a similar Na to Cl ratio to seawater, the correction using Equation 16 may still apply. However, we took additional steps to remove data where we suspected additional sources of Na beyond silicate mineral dissolution and rain water.

Using the catchment metadata associated with the GloRiCh database, we identified and removed sites known to be underlain by evaporite deposits ($n = 209$). The lithologic data used in GloRiCh is from Hartmann and Moosdorf (2012) and is mostly based on 1:1000000 scale geologic maps. While an enormous resource, this global lithologic map does not include exhaustive information about accessory phases within geologic units (e.g., evaporite minerals hosted in other rock types). Additionally, as it is based on surficial geology, the global lithologic map of Hartmann and Moosdorf (2012) does not constrain the presence of evaporite deposits in the shallow subsurface. Consistent with this, Cl concentrations in the GloRiCh database remain elevated even after sites with mapped evaporite deposits are removed. Specifically, the median of the culled dataset is 629 μM with a minimum and maximum of 0.03 (Madeira River at Porto Velho, Rondônia, Brazil) and $1.5{\cdot}10^6$ μM (Salt Fork Brazos River, Texas, USA), respectively. It is unlikely that the high end of this range can be generated by the evaporative enrichment of rainwater as rainwater Cl concentrations do not typically exceed 140 μM (Vet et al., 2014) and, for typical evapo-transpiration rates, enrichment factors should not exceed a factor of $\sim$100. Based on this assessment, we also removed sites where any reported Cl concentration exceed $1.4{\cdot}10^4$ μM as these sites likely require additional Cl sources beyond rainwater that should also affect the Na budget.

After sub-sampling the GloRiCh database as described above, we fitted the relationships between discharge and $[Na]$, $[Na]_{sil}$, and $[Si]$ data using a power law model (Equation 2). We utilized the trust-region non-linear fitting algorithm for the C-Q data with bisquare weighting to minimize the influence of outliers. The regression analysis was completed using the MATLAB 2020a curve-fitting toolbox.

We restricted our analysis to sites with greater than 10 pairs of concentration and discharge data for each element, which is less stringent than the requirement of 20 pairs used by Ibarra et al. (2017) and Godsey et al. (2019). Lastly, we discarded sites where the maximum discharge used in the fit was less than twice the minimum discharge used in the fit. All of the constraints listed above resulted in 1324, 1145, and 1224 sites where fits could be calculated for Na-Q, Si-Q, and Na_{sil}-Q, respectively. Fits for both Na and Si or both Na_{sil} and Si could be determined for 1140 and 1048 of these sites, respectively. For comparison, the analyses of Moon et al. (2014) and Ibarra et al. (2017) included only 43 sites whereas Godsey et al. (2019) included $\sim$2000 sites.

3 Results

3.1 Hydrologic model dynamics

3.1.1 Rainfall-runoff relationships

The clustering analysis utilized to parse the 2BK model simulations broadly identified models that differed in their rainfall-runoff relationships (Figures 2a-3a). Variations exist in the amplitude of the seasonal cycle of discharge as well as the short-term discharge response to storm events. Adopting typical hydrologic terminology, we refer to the different timescales of response as baseflow (low frequency variability) and quick flow (high frequency variability).

Differences between sets of model parameters for the behaviors of the baseflow and quick flow components are apparent in the outputs using all three input time-series. For brevity, we show only the results using the Smith River (Figure 2) and Bisley (Figure 3) inputs in the main text, but include an analogous figure for the Broad River input time-series in the Supplementary Material (Figure S1).

Clusters *iii* and *x* in Figure 2a show similarly damped quick flow variability, but differ in terms of the amplitude of the seasonal cycle of baseflow (the amplitude in cluster *iii* is greater than in cluster *x*). In general, simulations that produced higher amplitude quick flow variations showed a lower contribution from baseflow (i.e., the minimum Q for cluster *i* is lower than for cluster *x* in Figure 3a). However, some parameter combinations produced similar baseflow responses and differed only in their quickflow response (e.g., compare clusters *vii* and *ix* in Figure 3a).

The clustering analysis also identified differences in the seasonal cycle of tracer concentrations (Figures 2b-3b). Generally, clusters that show high amplitude quick flow variations also show a high amplitude seasonal cycle in tracer concentrations (e.g., compare clusters *i* and *x* in Figure 3). However, the cluster analysis also detected parameter combinations that produced broadly similar discharge responses, but different tracer dynamics. For example, clusters *vii* and *viii* in Figures 2 and 3 show different amplitudes in the tracer response despite similar quick flow variability. The models also produce differences in the phasing of the seasonal cycle of tracer concentrations. For example, clusters *iv* and *v* in Figure 3 are similar in their discharge response, but show different timing for when the minimum tracer concentration occurs.

Altogether, these results demonstrate that our selected model runs represent a wide range of hydrological behaviors that might be expected in real catchments (see Jasechko et al., 2016; Brunner et al., 2020, for comparison).

3.1.2 Time-variable transit time distributions

Throughout this paper, we will discuss multiple summary statistics of the different age distributions from each simulation. In particular, we emphasize the difference between statistics calculated for (1) each decile of discharge individually versus (2) a discharge-weighted average of all the discharge bins. In an attempt to limit confusion, we will distinguish these summary statistics using the following symbols. Discharge-weighted means (μ) of all of the bins from a simulation will be denoted by the subscript Q. Means calculated for a single decile of discharge will be denoted with the subscripts 1-10. For example, μ_Q and μ_1 refer to the discharge-weighted mean transit time and the mean transit time for discharges within the first decile of the discharge distribution, respectively. As already established, dimensional quantities will be distinguished from their dimensionless counterparts using a superscript $*$.

For our ultimate C-Q analysis, we use the dimensionless transit time distributions extracted from the 2BK model to account for uncertainties in both the absolute ages of

river discharge and effective reaction rates in natural systems. However, we start by providing dimensional transit time values as they illustrate the model behavior. For all of our ninety 2BK model runs, μ_Q values range from 80 to 1349 days (0.2 to 3.7 years). Within a subset of 30 simulations run using the same input time-series, μ_Q values span a slightly narrower range (e.g., μ_Q between 80 and 741 days using the Bisley input). In general, μ_Q values are highest for the simulations using the Broad River input time-series while μ_Q values are lowest when using the Bisley input. The average and range of μ_1 (lowest discharge decile) values using the Smith River (SR), Broad River (BR), and Bisley (PR) input time-series are 834 (220-2124), 1118 (293-2314), and 549 (128 to 1373) days, respectively. Transit times decrease with increasing discharge such that μ_{10} show an average and range of 240 (67-590), 388 (111-995), and 208 (57-504) days for the SR, BR, and PR inputs, respectively. These ages are similar to previous estimates for small catchments (e.g., McMillan et al., 2012; Klaus et al., 2015; Benettin, Kirchner, et al., 2015), but are slightly shorter than estimates for large catchments (e.g., Maxwell et al., 2016).

The parameter combinations we tested using the 2BK model also produce different transit time shapes depending upon the input time-series. This is evident in the empirical cumulative distribution functions derived from the dimensionless transit time values (Figure 4). For example, one difference can be seen by comparing the conditional transit time distributions for the lowest 10% of river flows between the SR input time-series (Figure 4a) and the other two inputs (Figure 4d,g). Due to long periods of time each year where there is little rainfall, the SR input time-series produces multi-modal transit time distributions. Despite the differences at low discharge, all of the input time-series converge to similar age distributions at high discharge where μ^*_{10} is about 0.5 (i.e., half of the discharge-weighted mean transit time; Figure 5).

The 2BK model predicts changes in the shape of the transit time distribution with discharge for all of the parameter combinations tested here. Similarly, all of our model results yield a negative relationship between discharge and the conditional mean transit time (Figure 5). At low discharge ($<10^{th}$ percentile), TTD shapes are broad and contain modes at intermediate ages (Figure 4a,d,g). In contrast, at high Q ($>90^{th}$ percentile), TTD shapes are strongly skewed with large fractions of water younger than μ_Q being exported and a heavy-tail of ages much older than μ_Q (Figure 4c,f,i).

3.2 Weathering model dynamics

Our design and implementation of Equation 11 effectively requires that m, d be greater than or equal to 1, in part, due to numerical stability. As a consequence, all of our weathering model simulations show a strong decline in dissolution rates with increasing reaction progress (Figure 6a). Stated another way, none of our simulations reach the equilibrium concentration when t is equal to T_{eq} (see also Ameli et al., 2017). Instead, most simulations reach 90% of the equilibrium cation concentration once t is a factor of 5 to 10 times higher than T_{eq} (Figure 6a). As discussed in Section 2.1.5, this non-linearity does not necessarily need to represent a thermodynamic control as multiple mechanisms exist that could lead to a decrease in rates with increasing reaction progress under far-from-equilibrium conditions (Schott et al., 2009; Eiriksdottir et al., 2013). We also note that in the end-member case where solute release rates are constant in time (effectively, $m, d = 0$ and $[\mathrm{C}]_{eq} = \infty$), the C-Q relationships would have the same exponents as the relationships between the conditional mean transit time and Q (Equation 1), which are shown in panel b of Figure 5.

In previous models of Si-Q relationships (Maher, 2011; Maher & Chamberlain, 2014), equations for mineral dissolution and precipitation similar to Equations 5 and 6 were combined to describe the *net* release of Si during weathering. By considering mineral dissolution and precipitation separately, our weathering model predicts that Si^* can transiently exceed the equilibrium concentration for some model parameter combinations (Fig-

ure 6b). In our model, this occurs because, at low degrees of super-saturation, the kinetics of secondary mineral precipitation can be too slow to keep pace with primary mineral dissolution resulting in a continued increase in Si^*. As the degree of super-saturation increases, secondary precipitation rates eventually exceed primary mineral dissolution rates, which slow with increasing reaction progress, eventually allowing the system to relax back to the equilibrium concentration. We refer to concentrations of Si^* that exceed the equilibrium concentration and lead to a non-monotonic relationship between Si^* and t^* (or Si^* and C_+^*) as an Si overshoot. Technically, this feature is imposed by our formulation of the reaction kinetics (Equations 10-11) and is not guaranteed to manifest in other, more realistic representations of silicate weathering (see Section 4.2.1). Nevertheless, we include it here as a hypothesis for solute release in silicate weathering systems under a limited range of conditions.

3.3 Combined model C-Q dynamics

Combining the 2BK and weathering models yields a wide range of C-Q behavior (Figures 7 and 8). Some of the model C-Q relationships are well-approximated by a power law (i.e., approximately linear in plot with logarithmic x and y axes; Equation 2). Others model C-Q relationships that are concave down for both cation concentrations and Si^* with Si^* sometimes reaching its maximum value at an intermediate values of Q (Figure 7a). Despite the fact that not all of the model (or natural; Torres et al., 2015; Moatar et al., 2017) C-Q relationships are well-described by a single power law, we still use this approach to summarize our results as it captures the first order behavior of each C-Q relationship (i.e., the fitted value of b captures the sensitivity of C to changes in Q). However, we do note that other, more sophisticated, descriptors of C-Q relationships exist (e.g., Neira et al., 2020). In the supplementary materials, we show the b-exponents for C_+^* and Si^* for each hydrologic model (Figure S2), weathering model (Figure S3), and input time-series (Figures S4 and S5) separated by the four Da values. In the main text, we mostly focus on subsets of the model results that typify specific model behaviors.

Typically, Si^* changes less with increasing Q as compared to C_+^*. This is captured in the difference between b-exponents calculated for each power law fit (Equation 2) to the C_+^*-Q and Si^*-Q data. For example, the median b-exponent for Si^*-Q at each value of Da exceeds the median b-exponent for C_+^*-Q (Figure 8a). No combinations of parameter values returned models where the value of b for Si^* was lower than for C_+^* (Figure 8a). However, some model results returned b-exponents for C_+^* and Si^* that are very similar (Figure 8a). For a single value of Da and one set of weathering model parameters, the values of the b exponent for C_+^*-Q and Si^*-Q relationships vary depending upon the hydrologic model used (Figures 7a,c). The variability due to different 2BK model parameter sets can be large (e.g., the values of b for C_+^*-Q ranging from -0.51 to -0.08 in Figure 7a,c). Similarly, when different input time-series are used, but all other model parameter values are held constant, the model generates different C-Q relationships (Figures 7d,e, S4 and S5) due to differences in the transit time distribution shapes between the input time-series (Figure 4).

The variability in b-exponents produced by the different 2BK model parameter sets is not solely due to the normalization by the discharge-weighted mean transit time and outliers in the TTDs. This is evidenced by similar ranges in b for constant Da and weathering model parameters if the TTDs are normalized by the discharge-weighted median or discharge-weighted trimmed mean transit time (Figure S6). While there is a slight effect of the normalization procedure (i.e., the different normalization approaches do not produce the exact same b exponents), it cannot account for the majority of the variation in C-Q relationships observed between different 2BK model parameters while other factors are held constant.

For a single value of Da, the distribution of b values for all combinations of weathering and hydrologic models are broad for fits to both C_+^*-Q and Si^*-Q relationships (Figure 8b,c). Though a few weathering models consistently produce lower b-exponents for C_+^* for all hydrologic models (Figure S3), much of the structure in the distribution of b values at a single value of Da is accounted for by varying the hydrological behavior via the 2BK model parameters (Figure S2).

The highest value of b that a set of hydrologic and kinetic models can produce depends on Da, with higher Da yielding higher values of b, all else held constant (Figure 8). Ultimately, at even higher values of Da, all fluid parcels should approach chemical equilibrium before being discharged, and b should collapse to 0, irrespective of the TTD shape. For the range of parameters we select, the value of b for Si^* can be significantly positive and reach as high as +0.28 (Figures 7c and 8c). Positive b exponents appear to be restricted to weathering models that generate maximum Si^* values of greater than 1.25 and increase as the max Si^* increases (Figure S7). At low Q, Si^* values for many C-Q relationships plateau at values above the equilibrium concentration. The lowest value of b produced by the model is for C_+^*-Q at a value of -3.36, which is lower than the value of -1 expected for simple dilution.

3.4 GloRiCh analysis

The calculated b exponents for Na-Q and Si-Q relationships from global rivers in the GloRiCh database show a range of values consistent with previous studies (Figure 8). Again, while our modelling approach represents a generic silicate cation, we focus on Na concentrations in the field data as Na is the easiest major cation to link directly to silicate weathering processes. Using just the best-fit estimates of b, a majority (95%) of b values for Na-Q relationships are between -0.57 and 0.01 with a median value of -0.20. After accounting for the proportion of Na sourced from atmospheric deposition, best-fit b values for Na_{sil}-Q relationships range from -0.83 to +0.06 (5th and 95th percentiles) with a median value of -0.24. For Si-Q relationships, 95% of b values are between -0.26 and +0.22 with a median value of -0.02. In addition to showing positive b values, some Si-Q relationships show peak concentrations at intermediate discharge values (Figure S8).

For sites where b exponents for both Na-Q and Si-Q could be determined, a majority (60%) returned exponents for Si that were significantly higher than the exponents determined for Na. Here, significance is defined as no overlap between the ranges defined by the 95% confidence intervals of each fitted b value. In contrast, only 4% of sites returned b exponents for Na that were significantly higher than b exponents for Si. This pattern was also present in the comparison between Na_{sil}-Q and Si-Q exponents with 60% of sites returning higher b exponents for Si-Q relationships and 4% returning higher b exponents for Na_{sil}-Q relationships.

4 Discussion

4.1 Relevance of the model predictions to natural systems

There are limits to how relevant any mechanism underlying the behavior of a model is to understanding a natural system. As we describe, our model approach reproduces a range of key behaviors observed in natural systems. However, that in and of itself does not necessarily mean that the mechanisms by which our model produces these behaviors are similar to those realized in nature. Accordingly, all of our discussion points must be prefaced by the caveat: if natural systems share similar properties to our model, then the explanation of our model system may be relevant to understanding field data.

The non-linear storage-discharge behavior of the 2BK model (Equations 3-4) is inspired by the recession behavior observed in natural systems and, as a result, the model

reproduces this feature of discharge time-series (Kirchner, 2009). The 2BK model also produces conservative tracer time-series that are amplitude damped and phase lagged relative to rainfall inputs in a similar manner to field measurements (Figures 2b and 3b; Kirchner, 2016b). Along these same lines, discharge-dependent changes in the shape of the transit time distribution predicted by the model, namely the property that a higher proportion of "young" water is exported at high discharge, are consistent with field measurements (Benettin, Kirchner, et al., 2015; Knapp et al., 2019) and more sophisticated hydrologic models (Wilusz et al., 2020). While additional complexity could be added to the 2BK model (e.g., by allowing η to vary with rainfall rate), the present formulation is sufficient to generate time-variable transit time distribution shapes. So long as any additional complexity does not cause there to be less variability in transit time distribution shape with discharge, then our general results and interpretations should hold.

The general formulation of the weathering model is broadly consistent with laboratory experiments and theory for reaction kinetics. For example, some degree of supersaturation is necessary to form secondary phases at an appreciable rate and multiple mechanisms exist that act to slow dissolution rates as reactions progress, including a thermodynamic control (Schott et al., 2009). Our weathering model is also consistent with the fact that river systems are typically super-saturated with a variety of secondary mineral phases (i.e., solute concentrations are typically above equilibrium concentrations; Ibarra et al., 2016).

It is also the case that our weathering model is missing features that are likely present in natural weathering systems. For example, rates of primary mineral dissolution and secondary mineral precipitation rates are not fully coupled in our model. Using aluminosilicate minerals as an example, it is expected that the activities of H^+, Al, and Si will appear in the thermodynamic terms (and also possibly the kinetic terms) for both the dissolving and precipitating mineral phases. So, if primary mineral dissolution rates are slow on account of near-equilibrium conditions, secondary mineral precipitation would act to increase dissolution rates (Maher et al., 2009), which is not directly represented in our model and could affect the appearance of an Si overshoot. This is discussed further in Section 4.2.1.

The C-Q relationships generated by our model, which range in shape from approximately power-law to concave down (Figure 7), are similar to the shapes observed in natural systems (e.g., Clow & Mast, 2010; Stallard & Murphy, 2014; Torres et al., 2015). Our model also captures the propensity for Si to be more chemostatic than cations like Na, which is observed in field data (Figure 8a). Lastly, our model generates positive and non-monotonic Si^*-Q relationships (Figures 7a), which are also observed in field data (Figure 8a,c S7), but have not been re-produced by previous reactive-transport models for C-Q behavior.

Despite being an over-simplification, our model generates a range of behaviors that are consistent with our knowledge of natural hydrologic systems and chemical weathering processes. Consequently, we are hopeful that the mechanisms identified in the subsequent analysis of our model are relevant for understanding some natural systems. However, we recognize that our assumption of a homogeneous distribution of reactive minerals is violated to varying degrees in natural systems, especially in catchments with well-developed soil profiles and/or mixed lithologies. Nevertheless, the assumption of homogeneity is a useful conceptual scenario to evaluate how much and what kind of C-Q variability can arise solely due to interactions between changes in transit time distribution shape and non-linear reaction dynamics. As such, our model results cannot refute the hypothesis that heterogeneity plays an important role in C-Q behavior. Instead, our results constrain the range of behaviors that can be produced by homogeneous systems, which is necessary to determine before any field data are interpreted as *requiring* Critical Zone heterogeneity.

4.2 Origin and significance of positive Si-Q relationships

4.2.1 Is an Si overshoot expected in natural systems?

A critical component underlying the ability of our model to generate positive Si-Q relationships is the weathering model formulation as it allows for an Si overshoot. Given that our weathering model is highly simplistic, it is not guaranteed that an Si overshoot can be generated in natural systems and/or more sophisticated models that account for solute speciation. To test whether or not added complexity prevents the formation of an Si overshoot, we developed an additional weathering model that simulates the dissolution of plagioclase feldspar and the formation of kaolinite/halloysite using expressions for Al and inorganic C speciation as well as more complete reaction rate law formulations. This additional "multi-component batch model" is described fully in Supplementary Text S1.

Using specific parameter combinations, the multi-component batch model is capable of producing an Si overshoot with an explicit coupling between primary mineral dissolution rates and secondary mineral precipitation rates. However, as with our more simplistic weathering model (Equations 10-11), the multi-component batch model also produces Si versus time relationships that lack an Si overshoot. While it is beyond the scope of this work to fully explore the parameter space of the multi-component batch model, it appears as if the behavior of Al is important in the generation of an Si overshoot in this more complex model. We find contrasting behavior between simulations where total Al concentrations are entirely regulated by feldspar dissolution and kaolinite/halloysite precipitation and simulations where Al concentrations are forced to be at low concentrations more typical of most natural waters. Specifically, the exact parameters necessary to generate an Si overshoot and what factors lead to the largest Si overshoot appear to be different depending on how Al concentrations vary in time.

Independent of our model analyses, we also note multiple previous models and experimental datasets that show non-monotonic relationships between the concentrations of silicate-derived solutes and reaction time. Reactive transport model simulations of coupled feldspar dissolution and kaolinite formation under hydrothermal conditions (65 and 100°C) by Yuan et al. (2017) show an Si overshoot depending upon the initial conditions and specified flow rate (see Figures 8,9 and 14 in Yuan et al., 2017). Hydrothermal (200 and 300°C) batch experiments of coupled feldspar dissolution and secondary formation by Zhu et al. (2010) show a small Si overshoot that is potentially within the analytical uncertainty of their measurements. However, they re-produce this feature using a numerical model and accounts for fluid speciation and uses full rate law formulations (Zhu et al., 2010). The work by Pohlmann et al. (2016) reports solute concentrations in porewaters from an experimental basaltic "watershed". These data show a non-monotonic relationship between porewater sampling depth and Si concentrations, which might be reflective of an Si overshoot if depth and time are equated as would be the case in a column reactor.

Altogether, we present the idea of an Si overshoot as a hypothesis for some of the positive (Figure 8) and non-monotonic (Figure S7) Si-Q relationships observed in field data. The experimental data available to test this hypothesis either represent different types of systems than natural watersheds (Zhu et al., 2010) or lack constraints on some key parameters (Pohlmann et al., 2016). As such, new, targeted data from laboratory or field systems would be useful. The available numerical models also have limited diagnostic ability on account of a lack of experimental constraints on the pH-dependence of clay mineral precipitation rates over the pH range of natural waters (Nagy et al., 1991; Yang & Steefel, 2008), outstanding uncertainties in the formulation of near-equilibrium rate laws (Schott et al., 2012), and the approximately order-of-magnitude uncertainty in experimentally-derived rate laws (e.g., Rimstidt et al., 2012). The effects of these uncertainties are explored in Supplementary Text S1.

4.2.2 Role of transit time in generating positive Si-Q relationships

Assuming that an Si overshoot is realistic feature, it worth noting that, using the same weathering model parameters, not all 2BK model parameter sets produce the same maximum (positive) Si^*-Q b-exponent. This highlights an important interaction between weathering geochemistry and hydrology necessary for a reactive-transport explanation of increasing Si^* with increasing discharge. To first order, the weathering model can be thought to generate three types of fluids with regards to dissolved silica: under-saturated waters (Si^* <1), super-saturated waters (Si^* >1), and equilibrated waters (Si^* ≈1; Figure 6b). These three fluid types relate to the water age where under-saturated fluids are the youngest, equilibrated waters are the oldest, and super-saturated waters have an intermediate age between the other two end-members. Thus, the Si^* of discharge can be thought of as being set by the relative contributions of these three end-member fluid types, which in turn are related to the transit time distribution.

All of the hydrologic model simulations show a decrease in the conditional mean transit time with increasing discharge (Figures 4,5). This constraint limits the number of ways that the mixing ratios between under-saturated, super-saturated, and equilibrated fluids can change with discharge to produce a positive Si^*-Q relationship, since each fluid type exists over an exclusive age range. Obeying this constraint, a positive Si^*-Q relationship is formed when, with increasing discharge, (1) the proportion of super-saturated fluids (intermediate ages) increases relative to equilibrated fluids (older ages) and (2) the concomitant increase in the proportion of under-saturated fluids (youngest ages) at high discharge does not dilute Si^* below the values produced at low discharge. This can be visualized as a shift from right to left along the horizontal axis of Figure 6b with increasing discharge, far enough into the "overshoot" zone but not far enough to where the curves decrease towards $Si^* = 0$. These conditions can be met when there is a strong overlap in the age range exported at high flow and the age range where Si^* is super-saturated, which is the case for our model simulations where Da is 10 or 100.

4.3 Apparent end-member mixing behavior

In addition to explaining positive Si^*-Q behavior, the analogy of three end-member fluid types also serves to emphasize that our model produces end-member-mixing-like relationships in scatter plots of C_+^* versus Si^* (Figures 6c and 9). Both C_+* and Si^* start at a value of 0 and end at a value of 1 (Figure 6). The curve connecting these points has a variable shape between model parameter sets ranging from nearly linear to non-monotonic (but unimodal; Figure 6c). For a given weathering model, the mixing of flow paths with varying transit time distributions produces fluids that plot in the space between each curve in Figure 6c and a straight line connecting the start and end points of the model (i.e., [0,0] and [1,1]), which gives the appearance of a three (or greater) end-member mixing relationship (Figure 9a,b). We note that this apparent end-member mixing behavoir is not restricted to weathering models that generate a large Si overshoot and instead require only that one solute reaches its equilibrium value well before the other.

While our model generates relationships that appear similar to end-member mixing, this behavior is unlike "true" end-member mixing where the concentration of each solute (or a set of concentration ratios) is fixed for each end-member. Fixed end-member compositions are inconsistent with our model as we assume that solute concentrations and concentration ratios vary continuously with time until an equilibrium is reached. Though it might be reasonable to assume that different age classes of water are vertically stratified in hillslope aquifers such that they can be separated into distinct end-members (Harman & Kim, 2019), it is not necessary to assume that the solid-phase substrate each fluid end-member is in contact with has a unique geochemical signature in order to produce the end-member-mixing-like behavior observed in hydrochemical datasets such as Figure 9c,d. Instead, temporal change in net reaction rates and time-variable transit time distribu-

tions create similar patterns in our model where the solid-phase composition is completely homogeneous.

For comparison to the modelled mixing relationships, we show data from Torres et al. (2015) and Torres et al. (2016), which come from a pair of nested catchments in the Peruvian Andes (Figure 9c,d). This dataset includes the mainstem of the Kosñipata River sampled at upper and lower gauging stations (Wayqecha and San Pedro) as well as tributary sub-catchments and groundwater seeps throughout the entire 161 km^2 watershed. A majority of the catchment is underlain by the same metasedimentary rock type, which outcrops at the surface. As a result, we expect our model assumption of homogeneous mineral reactivity to be reasonably appropriate for this setting.

To first order, the Andean data plot in the mixing space predicted by our modelling framework. In this interpretation, the tributary sub-catchments and groundwater seeps represent different transit time distribution shapes relative to the mainstem, but are otherwise generated via the chemical weathering the of the same minerals with similar, but unconstrained, kinetic parameters (Figure 9c,d). The differences between the samples from the upper and lower gauging stations suggests that the fluids discharged from the upper sub-catchment are more equilibrated (Figure 9c,d). This is consistent with data from Clark et al. (2014) that suggest that the upper sub-catchment has a lower fraction of "young" water (i.e., water with a transit time of less than $\sim$3 months Kirchner, 2016a) relative to the lower sub-catchment. However, these observations of longer fluid residence times and more equilibrated fluids do not apparently translate into more chemostatic Na-Q behavior as the b-exponent is lower (less chemostatic) in the upper sub-catchment relative to the lower sub-catchment (-0.33 $\pm$ 0.04 v.s. -0.23 $\pm$ 0.02; Torres et al., 2015). This unexpected disconnect between Da and C-Q behavior may relate to the hydrologic behavior of each catchment. For example, in Figure 8, some of the b-exponents from the Da = 10 simulations exceed those from the Da = 100 simulations on account of differences in transit time distribution shapes and how they vary with discharge. While an exact explanation for the difference in C-Q behavior in this dataset from Peru remains beyond the scope of this study, our cursory analysis hints at a more complex relationship between C-Q behavior and mineral reactivity than initially expected (c.f. Maher & Chamberlain, 2014).

4.4 Role of TTD shape in setting C-Q relationships

Different parameter sets for the 2BK hydrologic model can generate significant variability in C-Q relationships while both Da and the parameters of the weathering model are held constant (Figures 7 and 8). This is due to differences in how conditional transit time shapes vary with discharge between sets of hydrologic model parameters. As natural watersheds differ in how TTDs change with discharge (Harman, 2015; Benettin, Bailey, et al., 2015; Knapp et al., 2019; Wilusz et al., 2020), our model predictions imply that some of the observed variability in C-Q relationships (Figure 8) may arise from hydrologic processes in addition to differences in the abundance and reactivity of various primary minerals (Maher & Chamberlain, 2014; Ibarra et al., 2016).

Though time-variable TTDs influence C-Q behavior, there still are meaningful differences between model simulations with different Da values (Figure 8). Specifically, median b exponents increase with increasing Da over the range we test (Da from 0.1 to 100; Figure 8a). Assuming that this model prediction for C-Q relationships is accurate, it suggests that Da might be greater than 1 for many natural systems as this would explain the commonality of chemostatic behavior, the rarity of dilution behavior, and the occurrence of positive Si-Q relationships. Such an interpretation is also consistent with the rapid increases in solute concentrations observed for rainfall infiltrating into soil and regolith (Kim et al., 2014).

More precisely defining Da in natural systems based on C-Q may be more challenging, however. In our simulations, we find significant overlap in the distributions of b exponents as we vary Da over three orders of magnitude (Figure 8). In addition to overlapping with each other, the different model simulations also all overlap with field data (Figure 8). Furthermore, once reaction rates greatly exceed transit times, all fluid parcels will be at equilibrium such that b values are fixed at 0 and independent of additional increases in reaction rates. This equifinality in the relationship between Da and b values poses a major interpretive challenge, which, in principle, could be addressed in incorporating hydrologic constraints (e.g., young water fractions) into C-Q analysis (Benettin, Bailey, et al., 2015; Benettin et al., 2017; Luo & Jiao, 2019).

4.5 Implications for using C-Q theory in Earth System Models

To apply C-Q theory to Earth System Models, it is often assumed that C-Q relationships are spatially variable (e.g., set by the local tectonic uplift rate), but temporally constant over long ($>10^4$ years) timescales (Von Blanckenburg et al., 2015; Ibarra et al., 2016). With these assumptions, predicted changes in average runoff can be used to compute long-term changes in weathering fluxes. While this might be a necessary assumption given our incomplete understanding of the mechanisms underlying C-Q behavior, it is also likely an inaccurate assumption.

All else held constant, we find that different rainfall input time-series can generate different C-Q relationships (Figures 7d,e, S4, and S5). Though the 2BK model is highly simplified, it is not unreasonable to expect that the rate and pattern of rainfall inputs can influence water transit time distributions. The role of the rainfall input arises in our model from the assumption that water fluxes are a non-linear function of catchment storage. For example, catchment storage decreases substantially during periods with little to no rainfall in simulations run using the SR input time-series. This modifies the shape of the TTD at low discharge (Figure 4a,d,g), which in turn affects solute concentrations and C-Q relationships.

The possibility that rainfall patterns influence C-Q relationships is intriguing as it would modulate the sensitivity of weathering fluxes to climatic change by concomitantly changing solute generation efficiency alongside water fluxes. This could either amplify or dampen associated changes in weathering fluxes depending on how rainfall patterns are changed. However, a change in solute fluxes as a result of climatic forcing may not persist indefinitely or stay constant in magnitude as chemical weathering itself influences the structure of the Critical Zone. Changes in the porosity and thickness of the weathering zone affect the timescales of water storage and release (Harman & Cosans, 2019), which we document here to also influence C-Q relationships (Figure 7). Additionally, if solute fluxes are transiently increased such that the rate of primary mineral dissolution exceeds the rate of primary mineral supply from tectonic uplift, the system must evolve towards a C-Q relationship where solute fluxes satisfy long-term mass balance. Such behavior is not accounted for in our modelling framework, but instead, our work suggests that accurately incorporating it into future models will require a consideration of the co-evolution of mineral reactivity and fluid flow paths (Harman & Cosans, 2019).

The exact timescales over which C-Q relationships change in response to internal or external forcing remain poorly known, though long-term observations show that C-Q relationships have been stable in many catchments over the last few decades (Godsey et al., 2009). Constraining the response timescale of C-Q relationships underlies their utility in predicting how weathering fluxes will change in response to climatic forcing. By identifying additional drivers of C-Q behavior, namely time-variable TTDs, our study informs us which processes need to be better understood in order to advance C-Q theory. Specifically, it is important to constrain how changes in rainfall patterns influence C-Q through changes in TTD shape, as well as determining the timescales over which

TTDs evolve in response to changes in solute fluxes (i.e., catchment co-evolution; Troch et al., 2015).

5 Conclusions

By combining simple models of streamflow and coupled primary silicate mineral dissolution and secondary mineral precipitation, we are able to produce a wide range of C-Q relationships that encompasses much of the range observed in global rivers, including positive and non-monotonic Si-Q relationships. This result is intriguing given that we assume a homogeneous distribution of reactive minerals and instead generate C-Q variability through changes in transit time distribution shape with discharge and different non-linear reaction dynamics. While this finding does not necessarily mean that solid-phase heterogeneity in the Critical Zone does not play some role in C-Q relationships, it suggests that it is not required in many systems and may be difficult to separate from the expected temporal evolution. Along these same lines, our generation of positive Si-Q relationships arises from our specific and simplified assumptions about reaction dynamics and represents a testable hypothesis for weathering systems. We expect that other mechanisms for positive C-Q relationships are important in some systems, but caution that positive b exponents in and of themselves may not be diagnostic of specific processes (e.g., colloidal transport; Trostle et al., 2016; Aguirre et al., 2017).

We find a strong overlap in the C-Q relationships generated from different model runs where the ratio of the mean water transit time to maximum reaction timescales (i.e., the Damköhler number) was varied over three orders of magnitude. While we think that specific features of our model and global datasets imply that Damköhler numbers typically exceed 1 in natural settings (i.e., the prevalence of chemostasis, the rarity of simple dilution, and positive Si-Q relationships), more precise estimates will likely be challenging unless constraints on changes in water transit times, such as the discharge sensitivity of young water fractions (Benettin et al., 2017; Knapp et al., 2019) and/or other chronometers (Peters et al., 2014; Luo & Jiao, 2019), are directly incorporated into C-Q analysis.

We also find that different rainfall patterns can affect C-Q relationships through impacts on water storage and discharge. This result implies that assuming temporally constant C-Q relationships is problematic when incorporating C-Q theory into Earth System models. Since changes in chemical weathering affect water flow through the subsurface and vice versa, the evolution of C-Q relationships over time may be difficult to predict using modern observations or models, such as the one presented here, that do not account for catchment co-evolution and mass balance constraints imposed by mineral supply.

Acknowledgments

We acknowledge our data sources including the NSF Critical Zone Observatory Program. The Global River Chemistry Database is available at `doi.org/10.1016/j.proeps.2014.08.005`. All necessary model code and input data is available on the first author's GitHub page and will be archived on Zenodo after publication. Torres acknowledges support from the Sloan Foundation.

Parameter	Minimum	Maximum	Distribution
S_U^*	20	500	Log-uniform
S_L^*	500	10000	Log-uniform
β_U	1	20	Uniform
β_L	1	50	Uniform
η	0.01	0.9	Uniform

Table 1. Ranges of Hydrologic Model Parameters for Monte-Carlo Sampling

Parameter	Minimum	Maximum	Distribution
m, d	1	2	Uniform
m, p	1	2	Uniform
$\frac{[C_+]_{eq,d}}{\chi[Si]_{eq,p}}$	1	10	Uniform
R_p/R_d	0.1	100	Log-uniform

Table 2. Range of Weathering Model Parameters for Monte-Carlo Sampling

Hydrologic Model Parameter Selection

For each of 3 input time-series:

1. Pick random parameter set
2. Simulate discharge (Q) & tracer concentration

repeat 5000x

3. Identify 10 distinct model behavoirs

Result: 30 parameter sets (out of 15000 total)

Transit Time Distribution (TTD) Calculation

For each of 3 input time-series:

For each of 30 parameter sets:

1. Apply Monte-Carlo model
2. Bin daily TTDs by Q deciles

Result: 90 sets of 10 conditional dimensionless TTDs

Kinetic Model Parameter Selection

1. Pick random parameter set
2. Simulate C_+* and Si* as a function of t*

repeat 1000x

3. Identify 20 distinct model behavoirs

Result: 20 parameter sets (out of 5000 total)

C-Q generation

For each of 4 Damköhler Numbers:

For each of 90 sets of conditional dimensionless TTDs:

For each of the 20 kinetic model parameter sets:

1. Transform TTDs into distributions of C_+* & Si*
2. Calculate mean C_+* & Si* for each Q bin
3. Fit power law model to C_+*-Q and Si*-Q

Result: 7200 C-Q models with power law exponents for both C_+ and Si

Figure 1. Schematic overview of the modeling workflow employed in this study.

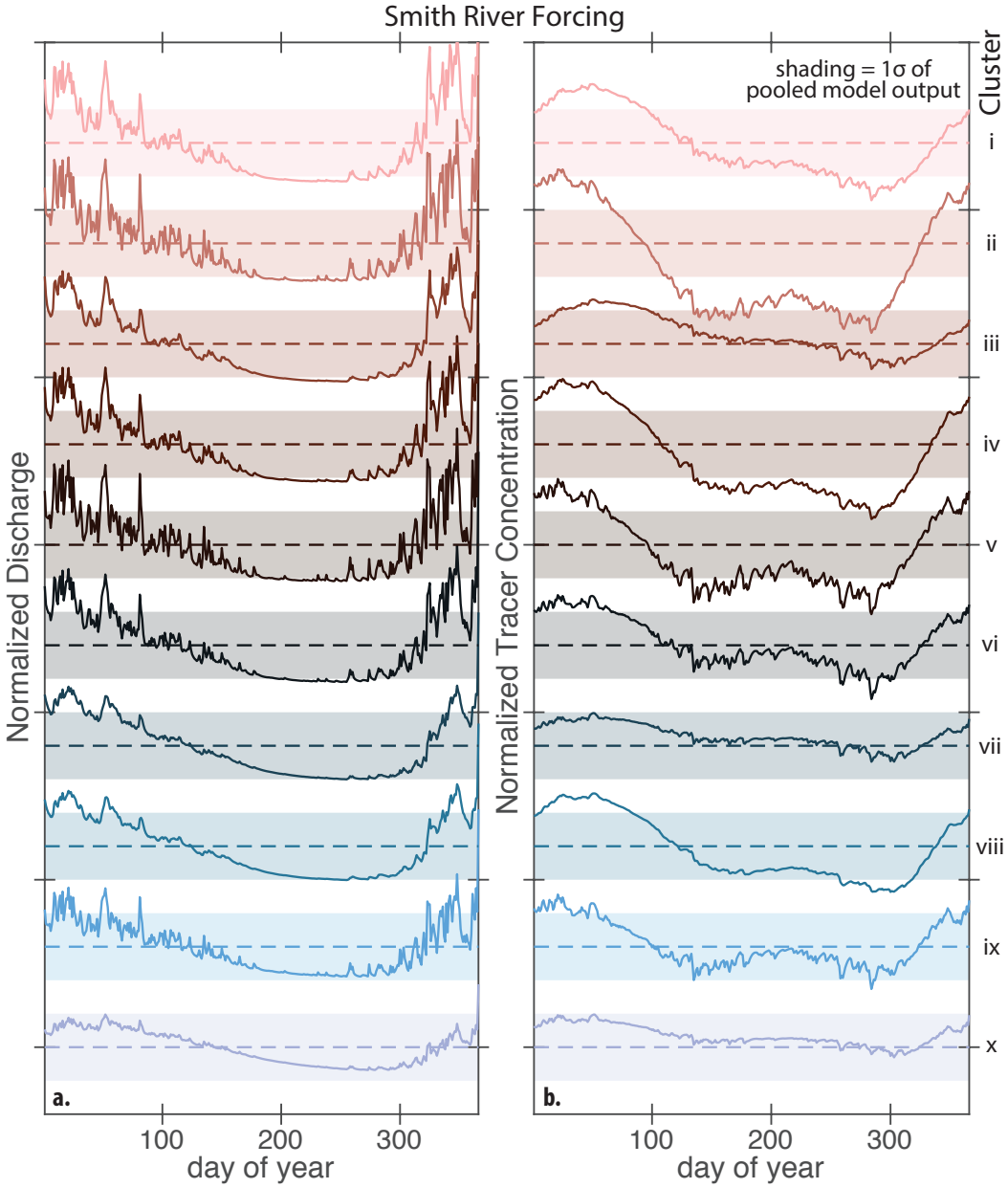

Figure 2. Clustered output from the 2BK model using the Smith River input time-series. (a) The annual cycle of daily average discharge. (b) The annual cycle of daily tracer concentrations. In both panels, the clusters are ordered and color-coded by the standard deviation of the discharge time-series. For each time-series, the dashed line indicates the annual mean for the entire 5000 member ensemble and the shaded band is one standard deviation for the entire 5000 member ensemble.

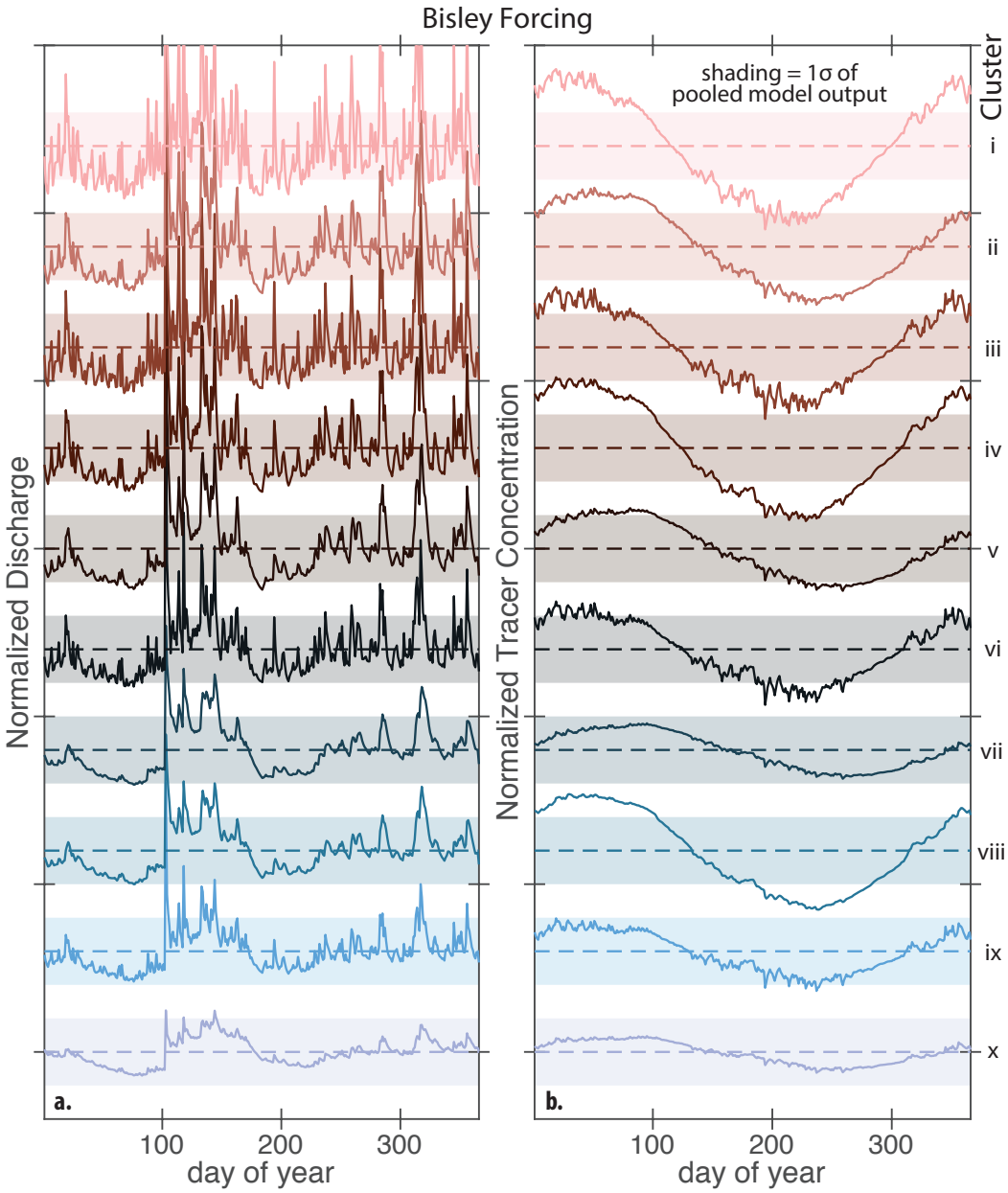

Figure 3. Clustered output from the 2BK model using the Bisley input time-series. (a) The annual cycle of daily average discharge. (b) The annual cycle of daily tracer concentrations. In both panels, the clusters are ordered and color-coded by the standard deviation of the discharge time-series. For each time-series, the dashed line indicates the annual mean for the entire 5000 member ensemble and the shaded band is one standard deviation for the entire 5000 member ensemble.

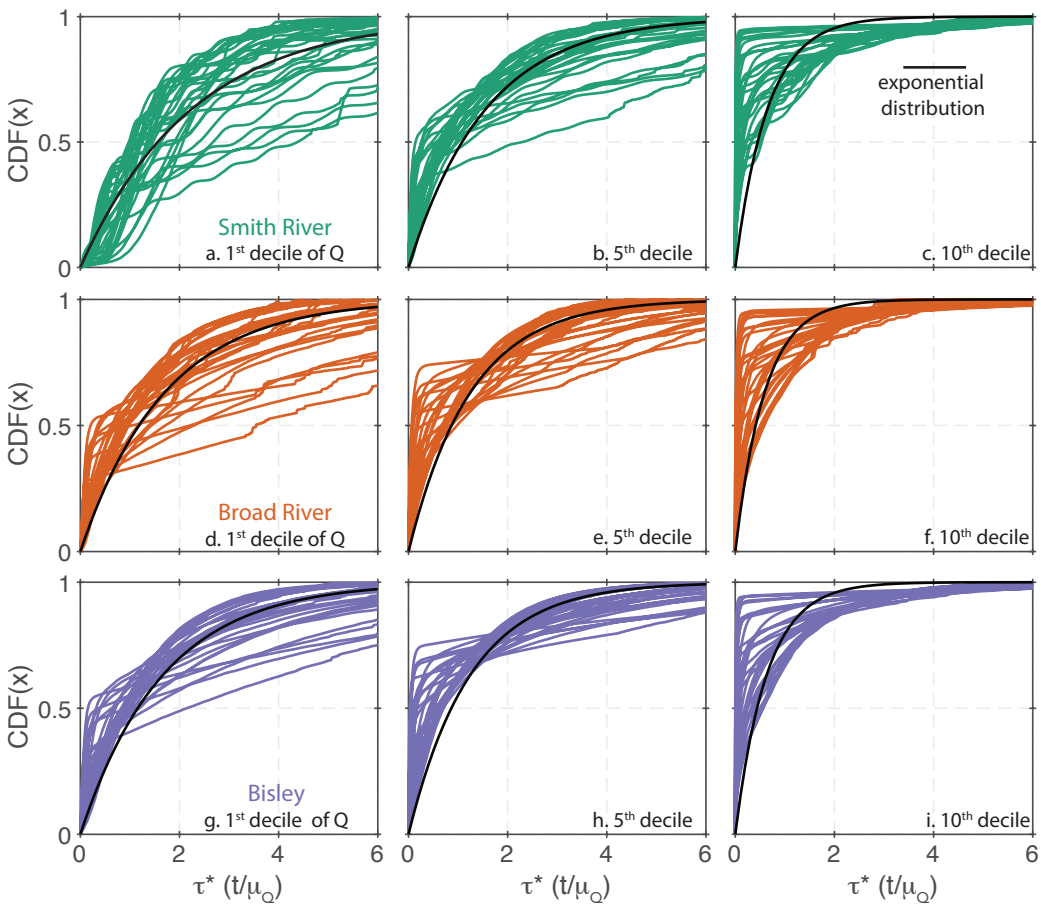

Figure 4. Conditional dimensionless transit time distributions. Each row of panels shows the cumulative distribution functions of transit times for the 1st, 5th, and 10th deciles of discharge for all hydrologic model parameters run with a single input forcing. Models run with the Smith River, Broad River, and Bisley inputs are shown in green, orange, and blue, respectively. For reference, the black lines show exponential transit time distributions with means equal to the average conditional mean for the TTDs from the hydrologic models.

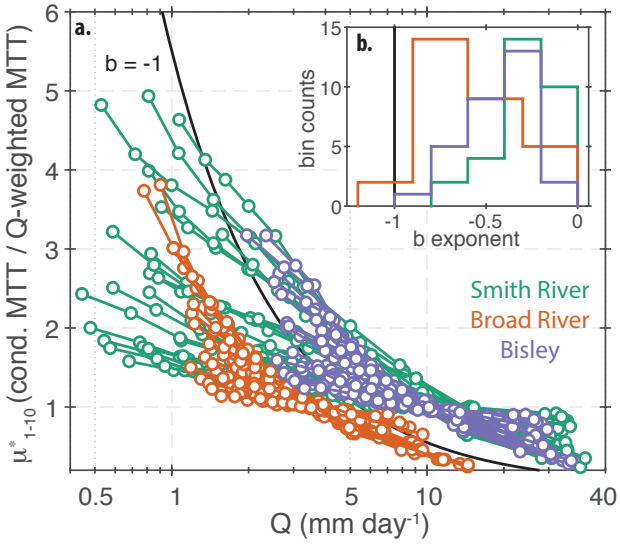

Figure 5. Model relationships between discharge and the conditional mean transit time for each decile of discharge. Models run with the Smith River, Broad River, and Bisley inputs are shown in green, orange, and blue, respectively. For reference, the black line shows an inverse relationship between discharge and conditional mean transit time. The inset panel b shows the best-fitting *b*-exponents from a power-law fit (Equation 2) to each transit time versus Q relationship.

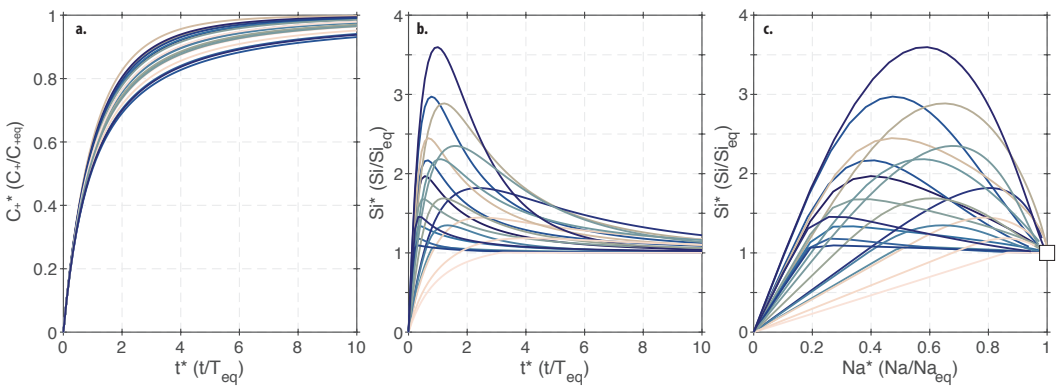

Figure 6. Different types of weathering model behavior identified using kmeans clustering, prior to coupling with the hydrologic 2BK model. Each line represents the potential evolution of a single water parcel as it gains and loses solutes through weathering reactions given a particular set of weathering model parameters (Table 2). (a) Normalized cation concentrations ($C_+^* = \mathrm{C}_+/\mathrm{C}_{+,eq}$) versus dimensionless weathering time ($\mathrm{t}/\mathrm{T}_{eq}$). (b) Normalized silicon concentrations ($Si^* = \mathrm{Si}/\mathrm{Si}_{eq}$) versus dimensionless weathering time. Note the "overshoot" of equilibrium concentrations (i.e., $\mathrm{Si}^* > 1$) produced by some model parameters. (c) Normalized silicon versus normalized cation concentrations. The square denotes the equilibrium end-point for all model simulations.

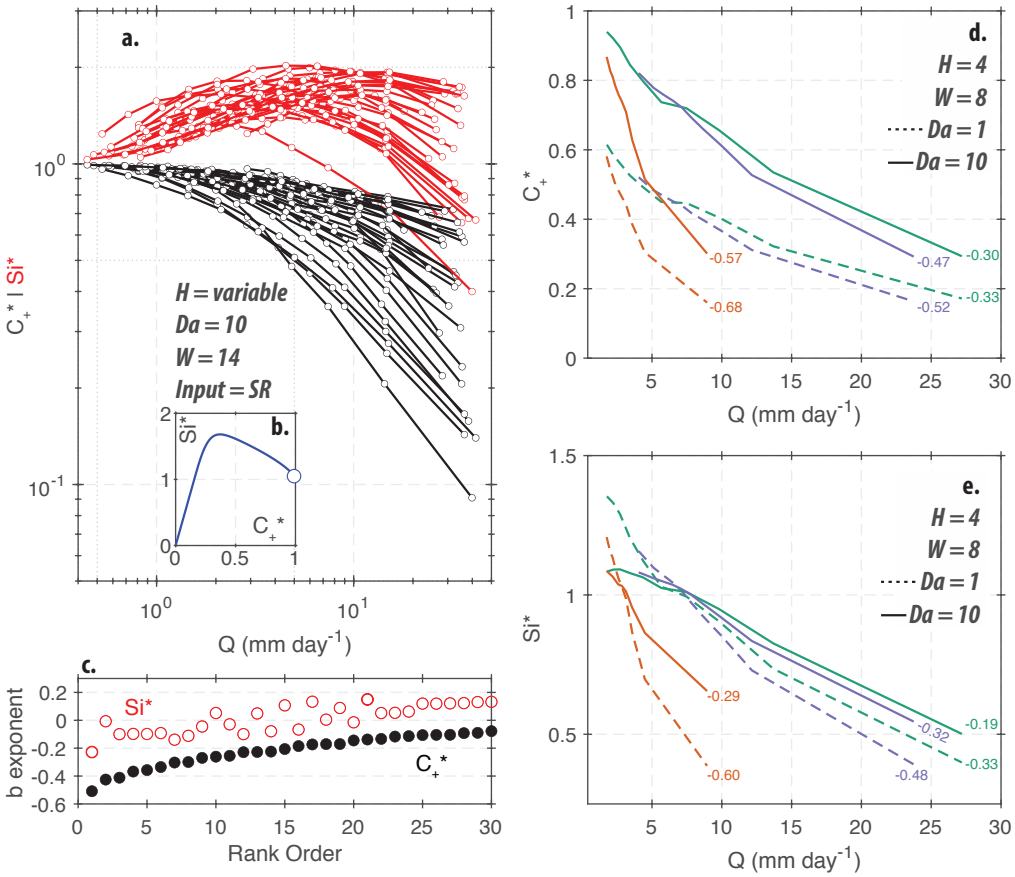

Figure 7. Combined 2BK and weathering model predictions of C-Q relationships. (a) C_+^*-Q (black) and Si*-Q (red) relationships for all 30 2BK model parameter sets (H) using a single input time-series (Input; Smith River), a single weathering model (W; parameter set 14), and a Damköhler number (Da) of 10. (b) The relationship between C_+^* and Si* predicted by weathering model parameter set 14. (c) Best fit *b*-exponents for the C-Q relationships shown in panel a. (d) Effect of different input time-series on C_+^*-Q relationships using 2BK model parameter set 4 and weathering model parameter set 8. Results using the Smith River, Broad River, and Bisley input time-series are shown in green, orange, and blue, respectively. Damköhler numbers of 1 and 10 are shown in dashed and solid lines, respectively. (e) Effect of different input time-series on Si*-Q relationships using 2BK model parameter set 4 and weathering model parameter set 8.

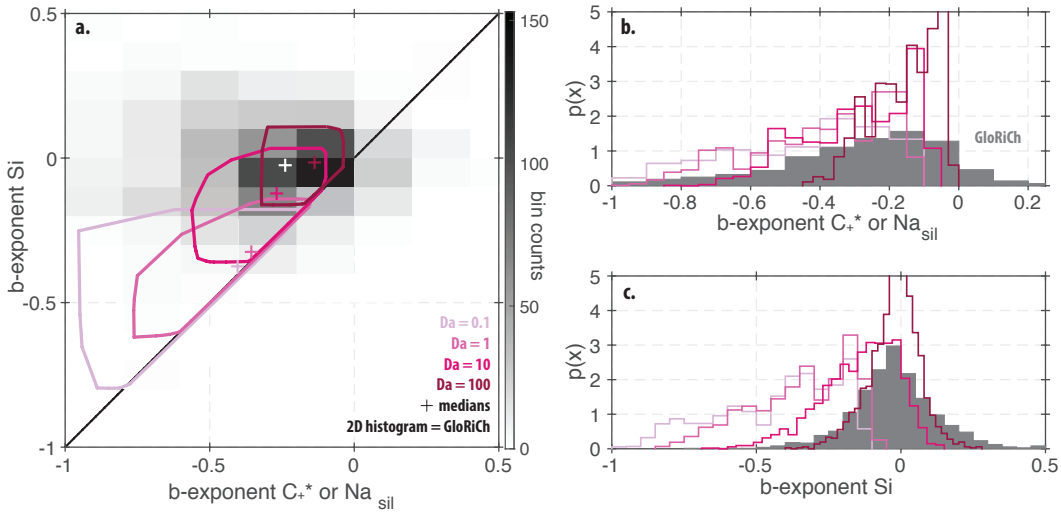

Figure 8. Field-measured (GloRiCh) and modelled C-Q relationships for all combinations of the weathering model and 2BK model parameter sets, rainfall input time-series, and Damköhler numbers. (a) Convex hulls around the 5th-95th percentile range of C^*_+-Q and Si^*-Q b-exponents produced by all combinations of the input time-series and model parameter sets, color-coded by Da. The gray-scale 2D histogram shows b-exponents for Si and Na_{sil} (Equation 16 calculated using the GloRiCh database. The crosses refer to median b-exponents for both the model and field data. (b) Probability density functions of best-fit b-exponents for C^*_+ (purple and red lines) and Na_{sil} (gray). (c) Probability density functions of best-fit b-exponents for Si^* (purple and red lines) and Si (gray).

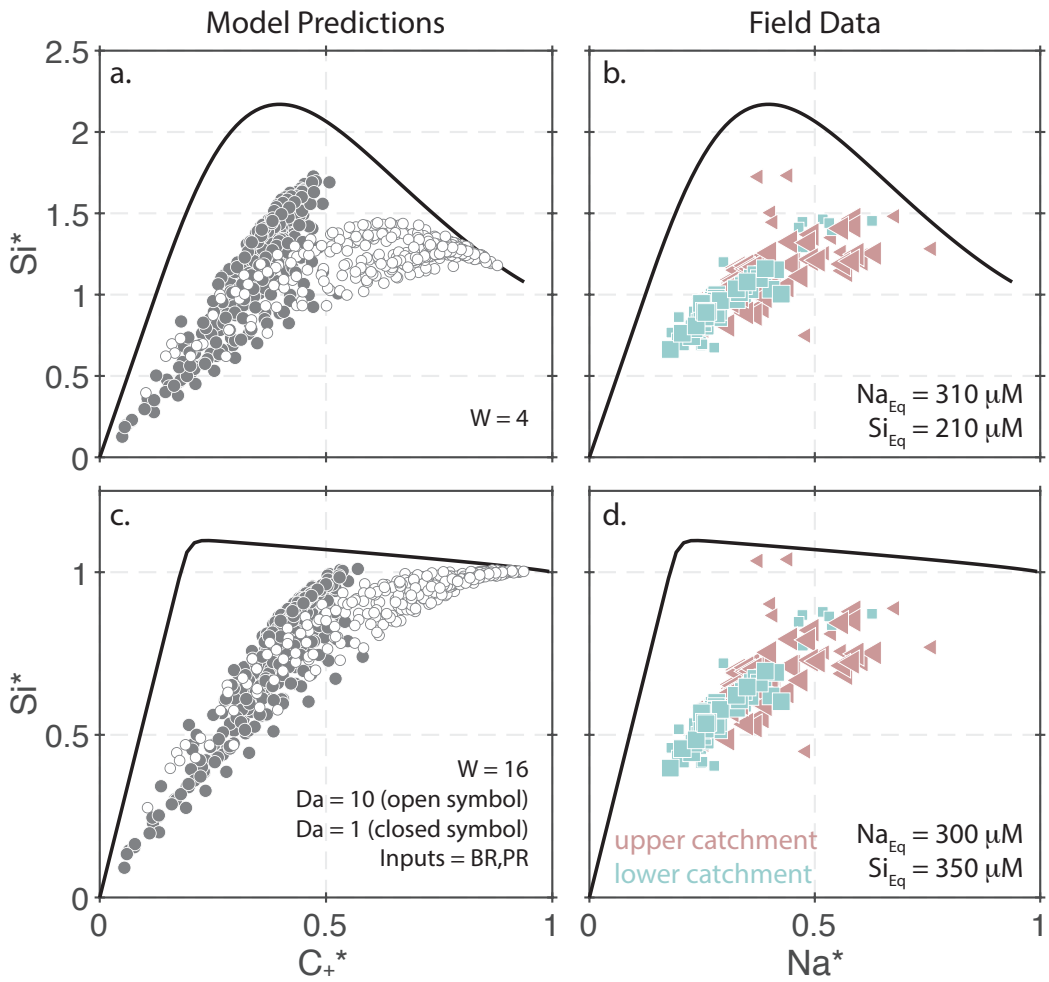

Figure 9. Weathering model reaction paths compared with binned model data field observations from Torres et al. (2015) and Torres et al. (2016). (a) The gray circles show the values of C_+^* and Si^* calculated for each discharge decile using weathering model parameter set 4 and all 2BK parameter sets with the Broad River and Bisley inputs. The closed and open symbols refer to simulations with Damköhler numbers of 1 and 10, respectively. The black solid line shows the reaction path for a single isolated flow path. (b) Same as in panel a, but with weathering model parameter set 16. (c-d) Same as in a and b, but with field data projected into the mixing space. The field data come from a pair of nested catchments. The pink and blue colored points refer to the upper and lower watersheds, respectively. The larger points refer to samples of the river mainstem whereas the smaller points are tributary sub-catchments or groundwater seeps. To project the field data into the mixing spaces defined by weathering model parameter sets 4 and 16, we used Na equilibrium concentrations of 310 and 300 μM and Si equilibrium concentrations of 210 and 350 μM, respectively.

References

Aguirre, A. A., Derry, L. A., Mills, T. J., & Anderson, S. P. (2017). Colloidal transport in the gordon gulch catchment of the boulder creek czo and its effect on c-q relationships for silicon. *Water Resources Research*, *53*(3), 2368–2383.

Ameli, A. A., Beven, K., Erlandsson, M., Creed, I. F., McDonnell, J. J., & Bishop, K. (2017). Primary weathering rates, water transit times, and concentration-discharge relations: A theoretical analysis for the critical zone. *Water Resources Research*, *53*(1), 942–960.

Anderson, S. P., Dietrich, W. E., Torres, R., Montgomery, D. R., & Loague, K. (1997, January). Concentration-discharge relationships in runoff from a steep, unchanneled catchment. *Water Resources Research*, *33*(1), 211.

Baronas, J. J., Torres, M. A., Clark, K. E., & West, A. J. (2017). Mixing as a driver of temporal variations in river hydrochemistry: 2. major and trace element concentration dynamics in the andes-amazon transition. *Water Resources Research*, *53*(4), 3120–3145.

Baronas, J. J., Torres, M. A., West, A. J., Rouxel, O., Georg, B., Bouchez, J., ... Hammond, D. E. (2018). Ge and si isotope signatures in rivers: A quantitative multi-proxy approach. *Earth and Planetary Science Letters*, *503*, 194–215.

Baronas, J. J., West, A. J., Burton, K. W., Hammond, D. E., Opfergelt, S., von Strandmann, P. A. E. P., ... Rouxel, O. J. (2020, Jan). *Ge and si isotope behavior during intense tropical weathering.* EarthArXiv. doi: 10.31223/osf.io/j5c8d

Benettin, P., Bailey, S. W., Campbell, J. L., Green, M. B., Rinaldo, A., Likens, G. E., ... Botter, G. (2015). Linking water age and solute dynamics in streamflow at the Hubbard Brook Experimental Forest, NH, USA. *Water Resources Research*(11), 9256–9272.

Benettin, P., Bailey, S. W., Rinaldo, A., Likens, G. E., McGuire, K. J., & Botter, G. (2017). Young runoff fractions control streamwater age and solute concentration dynamics. *Hydrological Processes*, *31*(16), 2982–2986.

Benettin, P., Kirchner, J. W., Rinaldo, A., & Botter, G. (2015). Modeling chloride transport using travel time distributions at Plynlimon, Wales. *Water Resources Research*, *51*(5), 1–18.

Bickle, M. J., Tipper, E. D., Galy, A., Chapman, H., & Harris, N. (2015). On discrimination between carbonate and silicate inputs to Himalayan rivers. *American Journal of Science*, *315*, 120–166.

Bolton, E. W., Berner, R. A., & Petsch, S. T. (2006). The weathering of sedimentary organic matter as a control on atmospheric o2: Ii. theoretical modeling. *American Journal of Science*, *306*(8), 575–615.

Bouchez, J., Moquet, J.-S., Espinoza, J. C., Martinez, J.-M., Guyot, J.-L., Lagane, C., ... Pombosa, R. (2017). River mixing in the amazon as a driver of concentration-discharge relationships. *Water Resources Research*, *53*(11), 8660–8685.

Bowen, G. J. (2008, March). Spatial analysis of the intra-annual variation of precipitation isotope ratios and its climatological corollaries. *Journal of Geophysical Research: Atmospheres*, *113*(D5), 1–10.

Brantley, S. L., Kubicki, J. D., & White, A. F. (2008). *Kinetics of water-rock interaction* (S. L. Brantley, J. D. Kubicki, & A. F. White, Eds.). New York: Springer.

Brunner, M. I., Melsen, L. A., Newman, A. J., Wood, A. W., & Clark, M. P. (2020). Future streamflow regime changes in the united states: assessment using functional classification. *Hydrology and Earth System Sciences*, *24*(8), 3951–3966.

Calmels, D., Galy, A., Hovius, N., Bickle, M., West, A. J., Chen, M.-c., & Chapman, H. (2011, February). Contribution of deep groundwater to the weathering budget in a rapidly eroding mountain belt, Taiwan. *Earth and Planetary Science Letters*, *303*(1-2), 48–58.

Cardinal, D., Gaillardet, J., Hughes, H. J., Opfergelt, S., & André, L. (2010). Contrasting silicon isotope signatures in rivers from the congo basin and the specific behaviour of organic-rich waters. *Geophysical Research Letters*, *37*(12), 1–6.

Chanat, J. G., Rice, K. C., & Hornberger, G. M. (2002). Consistency of patterns in concentration-discharge plots. *Water Resources Research*, *38*(8), 22–1.

Christophersen, N., Neal, C., Hooper, R. P., Vogt, R. D., & Andersen, S. (1990). Modelling streamwater chemistry as a mixture of soilwater end-members — A Step Towards Second-Generation Acidification Models. *Journal of Hydrology*, *116*, 307–320.

Clark, K. E. E., Torres, M. A. A., West, A. J. J., Hilton, R. G. G., New, M., Horwath, A. B. B., ... Malhi, Y. (2014). The hydrological regime of a forested tropical Andean catchment. *Hydrology and Earth System Sciences*, *18*(12), 5377–5397.

Clow, D. W., & Mast, M. A. (2010, January). Mechanisms for chemostatic behavior in catchments: Implications for CO2 consumption by mineral weathering. *Chemical Geology*, *269*(1-2), 40–51.

Daval, D., Hellmann, R., Corvisier, J., Tisserand, D., Martinez, I., & Guyot, F. (2010, May). Dissolution kinetics of diopside as a function of solution saturation state: Macroscopic measurements and implications for modeling of geological storage of CO2. *Geochimica et Cosmochimica Acta*, *74*(9), 2615–2633.

Derry, L. A., Kurtz, A. C., Ziegler, K., & Chadwick, O. A. (2005). Biological control of terrestrial silica cycling and export fluxes to watersheds. *Nature*, *433*(7027), 728–731.

Diamond, J. S., & Cohen, M. J. (2018). Complex patterns of catchment solute–discharge relationships for coastal plain rivers. *Hydrological Processes*, *32*(3), 388–401.

Dove, P. M., Han, N., & De Yoreo, J. J. (2005). Mechanisms of classical crystal growth theory explain quartz and silicate dissolution behavior. *Proceedings of the National Academy of Sciences*, *102*(43), 15357–15362.

Dralle, D., Karst, N., & Thompson, S. E. (2015). a, b careful! Consequences of scale invariance in power-law models of the streamflow recession. *Geophysical Research Letters*, *42*, 9285–9293.

Ebelmen, J. J. (1845). Sur les produits de la décomposition des especes minérales de la famille des silicates. *Annales des Mines*, *7*, 3–66.

Eiriksdottir, E. S., Gislason, S. R., & Oelkers, E. H. (2013, April). Does temperature or runoff control the feedback between chemical denudation and climate? Insights from NE Iceland. *Geochimica et Cosmochimica Acta*, *107*, 65–81.

Frings, P. J., Clymans, W., Fontorbe, G., Christina, L., & Conley, D. J. (2016). The continental si cycle and its impact on the ocean si isotope budget. *Chemical Geology*, *425*, 12–36.

Frings, P. J., Clymans, W., Fontorbe, G., Gray, W., Chakrapani, G., Conley, D. J., & De La Rocha, C. (2015). Silicate weathering in the Ganges alluvial plain. *Earth and Planetary Science Letters*, *427*, 136–148.

Gaillardet, J., Dupré, B., Louvat, P., & Allegre, C. J. (1999). Global silicate weathering and CO2 consumption rates deduced from the chemistry of large rivers. *Chemical Geology*, *159*(1-4), 3–30.

Gaillardet, J., Rad, S., Rivé, K., Louvat, P., Gorge, C., Allègre, C. J., & Lajeunesse, E. (2011). Orography-driven chemical denudation in the lesser antilles: Evidence for a new feed-back mechanism stabilizing atmospheric CO 2. *American Journal of Science*, *311*, 851–894.

Georg, R. B., Reynolds, B. C., West, a. J., Burton, K. W., & Halliday, A. N. (2007). Silicon isotope variations accompanying basalt weathering in Iceland. *Earth and Planetary Science Letters*, *261*, 476–490.

Godsey, S. E., Aas, W., Clair, T. a., de Wit, H. a., Fernandez, I. J., Kahl, J. S., ... Kirchner, J. W. (2010, April). Generality of fractal 1/f scaling in catchment tracer time series, and its implications for catchment travel time distributions. *Hydrological Processes*, *24*(12), 1660–1671.

Godsey, S. E., Hartmann, J., & Kirchner, J. W. (2019). Catchment chemostasis revisited: Water quality responds differently to variations in weather and climate. *Hydrological Processes*, *33*(24), 3056–3069.

Godsey, S. E., Kirchner, J. W., & Clow, D. W. (2009). Concentration–discharge relationships reflect chemostatic characteristics of US catchments. *Hydrological Processes*, *1864*(May), 1844–1864.

Guinoiseau, D., Bouchez, J., Gélabert, A., Louvat, P., Filizola, N., & Benedetti, M. F. (2016). The geochemical filter of large river confluences. *Chemical Geology*, *441*, 191–203.

Harman, C. J. (2015). Time-variable transit time distributions and transport: Theory and application to storage-dependent transport of chloride in a watershed. *Water Resources Research*, *51*(1), 1–30.

Harman, C. J., & Cosans, C. L. (2019). A low-dimensional model of bedrock weathering and lateral flow coevolution in hillslopes: 2. controls on weathering and permeability profiles, drainage hydraulics, and solute export pathways. *Hydrological processes*, *33*(8), 1168–1190.

Harman, C. J., & Kim, M. (2019). A low-dimensional model of bedrock weathering and lateral flow coevolution in hillslopes: 1. hydraulic theory of reactive transport. *Hydrological processes*, *33*(4), 466–475.

Hartmann, J., Lauerwald, R., & Moosdorf, N. (2014). A brief overview of the global river chemistry database, glorich. *Procedia Earth and Planetary Science*, *10*, 23–27.

Hartmann, J., & Moosdorf, N. (2012). The new global lithological map database glim: A representation of rock properties at the earth surface. *Geochemistry, Geophysics, Geosystems*, *13*(12).

Hellmann, R., & Tisserand, D. (2006). Dissolution kinetics as a function of the gibbs free energy of reaction: An experimental study based on albite feldspar. *Geochimica et Cosmochimica Acta*, *70*(2), 364–383.

Herndon, E. M., Dere, a. L., Sullivan, P. L., Norris, D., Reynolds, B., & Brantley, S. L. (2015). Landscape heterogeneity drives contrasting concentration–discharge relationships in shale headwater catchments. *Hydrology and Earth System Sciences*, *19*(8), 3333–3347.

Herndon, E. M., Steinhoefel, G., Dere, A. L., & Sullivan, P. L. (2018). Perennial flow through convergent hillslopes explains chemodynamic solute behavior in a shale headwater catchment. *Chemical Geology*, *493*, 413–425.

Hoagland, B., Russo, T. A., Gu, X., Hill, L., Kaye, J., Forsythe, B., & Brantley, S. L. (2017). Hyporheic zone influences on concentration-discharge relationships in a headwater sandstone stream. *Water Resources Research*, *53*(6), 4643–4667.

Hunsaker, C. T., & Johnson, D. W. (2017). Concentration-discharge relationships in headwater streams of the s ierra n evada, c alifornia. *Water Resources Research*, *53*(9), 7869–7884.

Ibarra, D. E., Caves, J. K., Moon, S., Thomas, D. L., Hartmann, J., Chamberlain, C. P., & Maher, K. (2016). Differential weathering of basaltic and granitic catchments from concentration–discharge relationships. *Geochimica et Cosmochimica Acta*, *190*, 265–293.

Ibarra, D. E., Moon, S., Caves, J. K., Chamberlain, C. P., & Maher, K. (2017). Concentration–discharge patterns of weathering products from global rivers. *Acta Geochimica*, *36*(3), 405–409.

Jasechko, S., Kirchner, J. W., Welker, J. M., & McDonnell, J. J. (2016). Substantial proportion of global streamflow less than three months old. *Nature Geo-*

science(January).

Johnson, N. M., Likens, G. E., Bormann, F. H., Fisher, D. W., & Pierce, R. S. (1969). A Working Model for the Variation in Stream Water Chemistry at the Hubbard Brook Experimental Forest, New Hampshire. *Water Resources Research*, *5*(6), 1353–1363.

Kaandorp, V., De Louw, P., van der Velde, Y., & Broers, H. (2018). Transient groundwater travel time distributions and age-ranked storage-discharge relationships of three lowland catchments. *Water Resources Research*, *54*(7), 4519–4536.

Kim, H., Bishop, J. K. B., Dietrich, W. E., & Fung, I. Y. (2014, September). Process dominance shift in solute chemistry as revealed by long-term high-frequency water chemistry observations of groundwater flowing through weathered argillite underlying a steep forested hillslope. *Geochimica et Cosmochimica Acta*, *140*, 1–19.

Kim, H., Dietrich, W. E., Thurnhoffer, B. M., Bishop, J. K. B., & Fung, I. Y. (2017). Controls on solute concentration-discharge relationships revealed by simultaneous hydrochemistry observations of hillslope runoff and stream flow: The importance of critical zone structure. *Water Resources Research*, *53*(2), 1424–1443.

Kirchner, J. W. (2009). Catchments as simple dynamical systems: Catchment characterization, rainfall-runoff modeling, and doing hydrology backward. *Water Resources Research*, *45*(2).

Kirchner, J. W. (2016a). Aggregation in environmental systems-part 1: Seasonal tracer cycles quantify young water fractions, but not mean transit times, in spatially heterogeneous catchments. *Hydrology and Earth System Sciences*, *20*(1), 279–297.

Kirchner, J. W. (2016b). Aggregation in environmental systems-part 2: Catchment mean transit times and young water fractions under hydrologic nonstationarity. *Hydrology and Earth System Sciences*, *20*(1), 299–328.

Kirchner, J. W., Feng, X., & Neal, C. (2000). Fractal stream chemistry and its implications for contaminant transport in catchments. *Nature*, *403*(6769), 524–527.

Klaus, J., Chun, K. P., McGuire, K. J., & McDonnell, J. J. (2015). Temporal dynamics of catchment transit times from stable isotope data. *Water Resources Research*, *51*(6), 4208–4223.

Knapp, J. L., Freyberg, J. v., Studer, B., Kiewiet, L., & Kirchner, J. W. (2020). Concentration-discharge relationships vary among hydrological events, reflecting differences in event characteristics. *Hydrology and Earth System Sciences Discussions*, 1–27.

Knapp, J. L., Neal, C., Schlumpf, A., Neal, M., & Kirchner, J. W. (2019). New water fractions and transit time distributions at plynlimon, wales, estimated from stable water isotopes in precipitation and streamflow. *Hydrology and Earth System Sciences*, *23*(10), 4367–4388. Retrieved from `https://www.hydrol-earth-syst-sci.net/23/4367/2019/` doi: 10.5194/hess-23-4367-2019

Kurtz, A. C., Lugolobi, F., & Salvucci, G. (2011, June). Germanium-silicon as a flow path tracer: Application to the Rio Icacos watershed. *Water Resources Research*, *47*(6), W06516.

Lee, T.-Y., Hong, N.-M., Shih, Y.-T., Huang, J.-C., & Kao, S.-J. (2017). The sources of streamwater to small mountainous rivers in taiwan during typhoon and non-typhoon seasons. *Environmental Science and Pollution Research*, *24*(35), 26940–26957.

Li, L., Bao, C., Sullivan, P. L., Brantley, S., Shi, Y., & Duffy, C. (2017). Understanding watershed hydrogeochemistry: 2. synchronized hydrological and geochemical processes drive stream chemostatic behavior. *Water Resources*

Research, *53*(3), 2346–2367.

Luo, X., & Jiao, J. J. (2019). Unraveling controlling factors of concentration discharge relationships in a fractured aquifer dominant spring-shed: Evidence from mean transit time and radium reactive transport model. *Journal of hydrology*, *571*, 528–544.

Maher, K. (2010, January). The dependence of chemical weathering rates on fluid residence time. *Earth and Planetary Science Letters*, *294*, 101–110.

Maher, K. (2011, December). The role of fluid residence time and topographic scales in determining chemical fluxes from landscapes. *Earth and Planetary Science Letters*, *312*(1-2), 48–58.

Maher, K., & Chamberlain, C. P. (2014, March). Hydrologic Regulation of Chemical Weathering and the Geologic Carbon Cycle. *Science*, *1502*.

Maher, K., Steefel, C. I., White, A. F., & Stonestrom, D. A. (2009, January). The role of reaction affinity and secondary minerals in regulating chemical weathering rates at the Santa Cruz Soil Chronosequence, California. *Geochimica et Cosmochimica Acta*, *73*(10), 2804–2831.

Maxwell, R. M., Condon, L. E., Kollet, S. J., Maher, K., Haggerty, R., & Forrester, M. M. (2016). The imprint of climate and geology on the residence times of groundwater. *Geophysical Research Letters*, *43*(2), 701–708.

McMillan, H., Tetzlaff, D., Clark, M., & Soulsby, C. (2012). Do time-variable tracers aid the evaluation of hydrological model structure? a multimodel approach. *Water Resources Research*, *48*(5).

Meybeck, M. (1987). Global chemical weathering of surficial rocks estimated from river dissolved loads. *American journal of science*, *287*(5), 401–428.

Moatar, F., Abbott, B. W., Minaudo, C., Curie, F., & Pinay, G. (2017). Elemental properties, hydrology, and biology interact to shape concentration-discharge curves for carbon, nutrients, sediment, and major ions. *Water Resources Research*, *53*(2), 1270–1287.

Möller, D. (1990). The na/cl ratio in rainwater and the seasalt chloride cycle. *Tellus B*, *42*(3), 254–262.

Moon, S., Chamberlain, C. P., & Hilley, G. E. (2014, June). New estimates of silicate weathering rates and their uncertainties in global rivers. *Geochimica et Cosmochimica Acta*, *134*, 257–274.

Moulton, K. L., West, J., & Berner, R. A. (2000). Solute flux and mineral mass balance approaches to the quantification of plant effects on silicate weathering. *American Journal of Science*, *300*(7), 539.

Nagy, K. L., Blum, A. E., & Lasaga, A. C. (1991). Dissolution and Precipitation Kinetics of Kaolinite at 80C and pH 3: The Dependence on Solution Saturation State. *American Journal of Science*, *291*, 649–686.

Neal, C., Robson, A., & Smith, C. J. (1990). Acid neutralization capacity variations for the hafren forest stream, mid-wales: inferences for hydrological processes. *Journal of Hydrology*, *121*(1-4), 85–101.

Neira, J. M. T., Andreassian, V., Tallec, G., & Mouchel, J.-M. (2020). A two-sided affine power scaling relationship to represent the concentration-discharge relationship. *Hydrology and Earth System Sciences*, *24*(4), 1823–1830.

Onderka, M., & Chudoba, V. (2018). The wavelets show it–the transit time of water varies in time. *Journal of Hydrology and Hydromechanics*, *66*(3), 295–302.

Peters, N. E., Burns, D. A., & Aulenbach, B. T. (2014). Evaluation of high-frequency mean streamwater transit-time estimates using groundwater age and dissolved silica concentrations in a small forested watershed. *Aquatic geochemistry*, *20*(2-3), 183–202.

Pohlmann, M., Dontsova, K., Root, R., Ruiz, J., Troch, P., & Chorover, J. (2016). Pore water chemistry reveals gradients in mineral transformation across a model basaltic hillslope. *Geochemistry, Geophysics, Geosystems*, *17*(6), 2054–2069.

Reeves, D., & Rothman, D. H. (2013). Age dependence of mineral dissolution and precipitation rates. *Global Biogeochemical Cycles*, *27*, 1–14.

Rimstidt, J. D., Brantley, S. L., & Olsen, A. A. (2012). Systematic review of forsterite dissolution rate data. *Geochimica et Cosmochimica Acta*, *99*(139), 159–178.

Ruiz, C. E. (2019). *Lczo – precipitation – throughfall – bisley – (1988-2015).* HydroShare. Retrieved from `http://www.hydroshare.org/resource/c635d74874544a72b1145324138b1956`

Samanta, A., Tripathy, G. R., & Das, R. (2019). Temporal variations in water chemistry of the (lower) brahmaputra river: Implications to seasonality in mineral weathering. *Geochemistry, Geophysics, Geosystems*, *20*(6), 2769–2785.

Schott, J., Oelkers, E. H., Bénézeth, P., Goddéris, Y., & François, L. (2012, November). Can accurate kinetic laws be created to describe chemical weathering? *Comptes Rendus Geoscience*, *344*(11-12), 568–585.

Schott, J., Pokrovsky, O. S., & Oelkers, E. H. (2009). The Link Between Mineral Dissolution/Precipitation Kinetics and Solution Chemistry. *Reviews in Mineralogy and Geochemistry*, *70*, 207.

Shiraki, R., & Brantley, S. L. (1995). Kinetics of near-equilibrium calcite precipitation at 100C: An evaluation of elementary reaction-based and affinity-based rate laws. *Geochimica et Cosmochimica Acta*, *59*(8), 1457–1471.

Stallard, R. F., & Edmond, J. M. (1981). Geochemistry of the Amazon 1. Precipitation chemistry and the marine contribution to the dissolved load at the time of peak discharge. *Journal of Geophysical Research*, *86*(C10), 9844–9858.

Stallard, R. F., & Murphy, S. F. (2014, December). A Unified Assessment of Hydrologic and Biogeochemical Responses in Research Watersheds in Eastern Puerto Rico Using Runoff–Concentration Relations. *Aquatic Geochemistry*, *20*(2-3), 115–139.

Stelzer, R. S., & Likens, G. E. (2006, January). Effects of sampling frequency on estimates of dissolved silica export by streams: The role of hydrological variability and concentration-discharge relationships. *Water Resour. Res.*, *42*(7), W07415.

Taylor, A. S., Blum, J. D., & Lasaga, A. C. (2000). The dependence of labradorite dissolution and Sr isotope release rates on solution saturation state. *Geochimica et Cosmochimica Acta*, *64*(14), 2389–2400.

Torres, M. A., Baronas, J. J., Clark, K. E., Feakins, S. J., & West, A. J. (2017). Mixing as a driver of temporal variations in river hydrochemistry: 1. Insights from conservative tracers in the Andes-Amazon transition. *Water Resources Research*, *53*(4), 3102–3119.

Torres, M. A., Moosdorf, N., Hartmann, J., Adkins, J. F., & West, A. J. (2017). Glacial weathering, sulfide oxidation, and global carbon cycle feedbacks. *Proceedings of the National Academy of Sciences*, *114*(33), 8716–8721.

Torres, M. A., Paris, G., Adkins, J. F., & Fischer, W. W. (2018). Riverine evidence for isotopic mass balance in the earths early sulfur cycle. *Nature Geoscience*, *11*(9), 661–664.

Torres, M. A., West, A. J., & Clark, K. E. (2015). Geomorphic regime modulates hydrologic control of chemical weathering in the andes–amazon. *Geochimica et Cosmochimica Acta*, *166*, 105–128.

Torres, M. A., West, A. J. J., Clark, K. E. K. E., Paris, G., Bouchez, J., Ponton, C., ... Adkins, J. F. J. F. (2016). The acid and alkalinity budgets of weathering in the Andes-Amazon system: Insights into the erosional control of global biogeochemical cycles. *Rapid Communications in Mass Spectrometry*, *450*, 381–391.

Troch, P. A., Lahmers, T., Meira, A., Mukherjee, R., Pedersen, J. W., Roy, T., & Valdés-Pineda, R. (2015). Catchment coevolution: A useful framework for improving predictions of hydrological change? *Water Resources Research*, *51*(7),

4903–4922.

Trostle, K. D., Runyon, J. R., Pohlmann, M. A., Redfield, S. E., Pelletier, J., McIntosh, J., & Chorover, J. (2016). Colloids and organic matter complexation control trace metal concentration-discharge relationships in marshall gulch stream waters. *Water Resources Research*, *52*(10), 7931–7944.

Vet, R., Artz, R. S., Carou, S., Shaw, M., Ro, C. U., Aas, W., ... Reid, N. W. (2014). A global assessment of precipitation chemistry and deposition of sulfur, nitrogen, sea salt, base cations, organic acids, acidity and pH, and phosphorus. *Atmospheric Environment*, *93*, 3–100.

Von Blanckenburg, F., Bouchez, J., Ibarra, D. E., & Maher, K. (2015). Stable runoff and weathering fluxes into the oceans over quaternary climate cycles. *Nature Geoscience*, *8*(7), 538.

Walker, J., Hays, P. B., & Kasting, J. F. (1981). A negative feedback mechanism for the long-term stabilization of the Earth's surface temperature. *Journal of Geophysical Research*, *86*(C10), 9776–9782.

Wilusz, D., Harman, C., Ball, W., Maxwell, R., & Buda, A. (2020). Using particle tracking to understand flow paths, age distributions, and the paradoxical origins of the inverse storage effect in an experimental catchment. *Water Resources Research*, e24397.

Winnick, M. J., Carroll, R. W., Williams, K. H., Maxwell, R. M., Dong, W., & Maher, K. (2017). Snowmelt controls on concentration-discharge relationships and the balance of oxidative and acid-base weathering fluxes in an alpine catchment, East River, Colorado. *Water Resources Research*, *53*(3), 2507–2523.

Wymore, A. S., Brereton, R. L., Ibarra, D. E., Maher, K., & McDowell, W. H. (2017). Critical zone structure controls concentration-discharge relationships and solute generation in forested tropical montane watersheds. *Water Resources Research*, *53*(7), 6279–6295.

Yang, L., & Steefel, C. I. (2008). Kaolinite dissolution and precipitation kinetics at 22 c and ph 4. *Geochimica et Cosmochimica Acta*, *72*(1), 99–116.

Yuan, G., Cao, Y., Gluyas, J., & Jia, Z. (2017). Reactive transport modeling of coupled feldspar dissolution and secondary mineral precipitation and its implication for diagenetic interaction in sandstones. *Geochimica et Cosmochimica Acta*, *207*, 232–255.

Zhi, W., Li, L., Dong, W., Brown, W., Kaye, J., Steefel, C., & Williams, K. H. (2019). Distinct source water chemistry shapes contrasting concentration-discharge patterns. *Water Resources Research*, *55*(5), 4233–4251.

Zhu, C., Liu, Z., Zhang, Y., Wang, C., Scheafer, A., Lu, P., ... Rimstidt, J. D. (2016). Measuring silicate mineral dissolution rates using si isotope doping. *Chemical Geology*, *445*, 146–163.

Zhu, C., Lu, P., Zheng, Z., & Ganor, J. (2010, July). Coupled alkali feldspar dissolution and secondary mineral precipitation in batch systems: 4. Numerical modeling of kinetic reaction paths. *Geochimica et Cosmochimica Acta*, *74*(14), 3963–3983.

Supporting Information for "Modulation of riverine concentration-discharge relationships by changes in the shape of the water transit time distribution"

Mark A. Torres[1], J. Jotautas Baronas [2]

[1]Department of Earth, Environmental, & Planetary Sciences, Rice University

[2]Department of Earth Sciences, University of Cambridge

Contents of this file

1. Text S1
2. Tables S1 to S3
3. Figures S1 to S13

Text S1. Multi-component batch model

1. Key Reactions

The dissolution reaction for plagioclase feldspar with a composition ranging from pure albite ($NaAlSi_3O_8$) to pure anorthite ($CaAl_2Si_2O_8$) can be written as:

$$\mathrm{Na}_x\mathrm{Ca}_{(1-x)}\mathrm{Al}_{(2-x)}\mathrm{Si}_{(2+x)}\mathrm{O}_8 + 4\,(2-\mathrm{x})\mathrm{H}^+ + (4\,\mathrm{x})\mathrm{H}_2\mathrm{O} \longrightarrow \mathrm{xNa}^+ + (1-\mathrm{x})\mathrm{Ca}^{2+} + (2-\mathrm{x})\mathrm{Al}^{3+} + (2+\mathrm{x})\mathrm{H}_4\mathrm{SiO}_4 \tag{1}$$

where x is the mole fraction of albite in the system (Gudbrandsson et al., 2014). The chemical reaction for the formation of kaolinite can be written as:

$$2\,\mathrm{Al}^{3+} + 2\,\mathrm{H}_4\mathrm{SiO}_4 + \mathrm{H}_2\mathrm{O} \longrightarrow \mathrm{Al}_2\mathrm{Si}_2\mathrm{O}_5(\mathrm{OH})_{4(\mathrm{s})} + 6\,\mathrm{H}^+ \tag{2}$$

Based on the aqueous species present in these reactions, it is necessary to account for the fluid pH and associated changes in the speciation of Al, Si, Na, and Ca in order to determine thermodynamic saturation states. At low ionic strength, it is reasonable to assume that Ca and Na remain dominantly as Na^+ and Ca^{2+}. At pH values of less than 9, Si should dominantly be speciated as H_4SiO_4. However, over a wider range in pH, Al is present as 5 species: Al^{3+}, $AlOH^{2+}$, $Al(OH)_2{}^+$, $Al(OH)_3$ and $Al(OH)_4{}^-$. For the dissolution-precipitation of aluminosilicates, it is necessary to predict the abundance of the Al^{3+} species in particular, which can be determined from the total Al concentration ($[Al]_T$) and fluid pH (assuming that activity coefficients are all equal to 1) with the equation:

$$[Al^{3+}] = \frac{[Al]_T}{1 + \frac{K_1}{(aH^+)} + \frac{K_2}{(aH^+)^2} + \frac{K_3}{(aH^+)^3} + \frac{K_4}{(aH^+)^4}} \tag{3}$$

where aH^+ is equal to 10^{-pH} and K_1-K_4 refer to the equilibrium constants for the formation of each of the 4 other dissolved Al species (ordered as written above; Drever et al., 1988).

To help predict the fluid pH, we assume weathering takes place in an open system with respect to CO_2 and that pCO_2 in weathering zone is elevated relative to the atmosphere as a result of biological respiration. The concentration of aqueous CO_2 ($H_2CO_3{}^*$) can be related to pCO_2 via:

$$H_2CO_3{}^* = K_H \cdot pCO_2 \tag{4}$$

where K_H is a Henry's Law volatility constant. At non-zero alkalinity concentrations, carbonic acid disassociates into bicarbonate ($HCO_3{}^-$) and carbonate ion ($CO_3{}^{2-}$). For bicarbonate ion, the relevant equilibrium reaction is:

$$H_2CO_3{}^* \longleftrightarrow H^+ + HCO_3{}^- \tag{5}$$

which has an equilibrium constant (K_i) equal to

$$K_i = \frac{[\mathrm{HCO_3}^-][\mathrm{H}^+]}{[\mathrm{H_2CO_3}^*]} \tag{6}$$

An analogous reaction and equilibrium constant (K_{ii}) can be written for the equilibrium between bicarbonate and carbonate ion.

If it is assumed that the concentrations of Na and Ca greatly exceed aluminum and that the concentration of HCO_3^- greatly exceeds the concentration of CO_3^{2-}, charge balance can be invoked to equate the sum of Ca^{2+} and Na^+ with HCO_3^- where:

$$[\mathrm{HCO_3}-] = [\mathrm{Na}^+] + 2\,[\mathrm{Ca}^{2+}] \tag{7}$$

This approximation can be combined with Equations 4 and 6 to generate an approximate relationship between cation concentrations and pH (expressed as aH^+) where:

$$\frac{1}{aH^+} = \frac{[Na^+] + 2[Ca^{2+}]}{K_i \cdot K_H \cdot pCO_2} \tag{8}$$

Together, Equations 1 and 3 allow for the approximate modelling of changes in fluid pH and aluminum speciation resulting from mineral dissolution/precipitation at constant pCO_2 assuming that all activity coefficients are equal to 1.

If aluminum concentrations are sufficiently high such that they a major component of charge balance, then the approach outlined above will underestimate the fluid pH. Incorporating aluminum into charge balance is complicated, however, by the fact that the net charge of aluminum also depends on pH. In the approach we take here, we perform one iteration where we calculate the pH from Na and Ca concentrations using equation 8, solve for aluminum speciation using Equation 3, update the pH by including the net aluminum charge in the charge balance determination of HCO_3^- (i.e., Equation 7), and lastly update the abundance of Al^{3+} using the new value for pH.

2. Dissolution Rate Laws

Published rate laws for plagioclase dissolution at constant temperature typically take the form of:

$$\text{Rate} = k_D \cdot \left(\frac{(aH^+)^3}{aAl^{3+}}\right)^N \cdot \left(1 - \exp\left(\frac{\Delta G}{\sigma RT}\right)^m\right)^n \tag{9}$$

where k_D is a dissolution rate constant, N is a modifier on the effect of fluid chemistry at far from equilibrium conditions, ΔG / σRT is a thermodynamic term, and m and n are exponents that modify the thermodynamic term (e.g., Eiriksdottir et al., 2013). Transition state theory (TST) predicts values of m and n equal to 1, though some experiments disagree with these predictions (e.g., Taylor et al., 2000; Arvidson & Luttge, 2010). Values for the other variables in Equation 9 have been determined using laboratory experiments. For example, Gudbrandsson et al. (2014) tested a range of compositions from An2 to An89 at far from equilibrium conditions and at a temperature of 22°C. In this publication, the authors present a rate law where the values of k_D and N vary depending upon whether the system is above or below a pH value of 6. Additionally, for pH values below 6, k_D and N were found to vary as a function of the mole fraction anorthite of the dissolving feldspar.

In a set of preliminary experiments, we found that implementing the Gudbrandsson et al. (2014) rate law led to numerical problems in simulations where the pH evolved from below to above 6 on account of the rapid change in rate law parameters. In order to avoid this problem, we re-fit their experimental data so that the resulting rate law was a smoother function of pH. Specifically, we separated the data based on the mole fraction anorthite (above 80% and below 20%) and, for each subset, fit a second order polynomial to the relationship between pH and the log-transform of the measured dissolution rate

(Figure S9a, Table S3). Such an approach obviously deviates from Equation 9 in that it does not include the activity of Al^{3+}. However, from Equation 3, it is clear that, for a constant total Al concentration, the activity of Al^{3+} varies as a function of pH. In this way, variations in the ratio of the H^+ activity to the Al^{3+} activity can be represented solely by pH so long as variations in total Al concentrations are relatively small (Figure S9b) and/or N is low (experimentally determined N values are between 0.07 to 0.36; Gudbrandsson et al., 2014).

It is important to note that our fit to the experimental data only explains a portion of the total variance in the dataset (Figure S9a). This is also true of the original fit presented in (Gudbrandsson et al., 2014) and the experimentally-derived rate laws for other silicate minerals (e.g., Rimstidt et al., 2012). Generally, the amount of unexplained variability is fairly large in that, at a given pH, experimental dissolution rates can vary by nearly an order of magnitude relative to what is predicted by the best-fit rate law (Figure S9a; Rimstidt et al., 2012). To account for this uncertainty, we also test additional polynomial equations that better describe the variation in the minimum measured dissolution rate as a function of pH (the dashed lines in Figure S9a). We focus on minimum rates here on account of well-known discrepancies between laboratory- and field-measured dissolution rates with laboratory values typically being too high (White & Brantley, 2003). Lastly, we note that our approach to separate the experimental data between anorthite and albite requires that, in our ultimate model formulation, we treat them as separate minerals as opposed to considering a single plagioclase mineral as a solid solution.

3. Precipitation Rate Laws

Experiments performed at a pH value of 4 and a temperature of 22°C by Yang and Steefel (2008) determined that kaolinite precipitation rates (R_P) either scaled linearly with ΔG:

$$R_P = k_P \cdot \frac{\Delta G}{RT} \tag{10}$$

or followed TST predictions:

$$R_P = -k_P \cdot \left(1 - \exp\left(\frac{\Delta G}{\sigma RT}\right)\right) \tag{11}$$

where k_P is a precipitation rate constant. The experiments that followed TST predictions were seeded with kaolinite that had been previously used in a long-term dissolution experiment. In the remaining experiments, the seed material was not dissolved prior to the start of the precipitation experiment. Intriguingly, the experiments with the pre-dissolved seed material did not display a TST-like thermodynamic dependence indefinitely and instead evolved to the linear behavior observed in other experiments seeded with less reacted kaolinite.

Unfortunately, there appear to be no experimental data that constrain the pH dependence of kaolinite precipitation above a pH of 4 as the only other kaolinite precipitation experiment we are aware of was conducted at a pH of 3 (Nagy et al., 1991; Perez-Fodich & Derry, 2020). Other clay minerals, such as greenalite ($(Fe^{2+}, Fe^{3+})_{(2-3)}Si_2O_5(OH)_4$), are purported to have precipitation rates that scale as $pH^{22.1}$ (Tosca et al., 2016; Isson & Planavsky, 2018). As such, there is reason to suspect the pH dependence of this reaction is important. Additionally, there appear to be no experimental data that constrain the

kinetics of halloysite precipitation, which is a polymorph of kaolinite thought form as a precursor phase and regulate solute concentrations (Maher, 2011).

4. Water-Rock Ratio

To account for mineral surface area as well as the fluid volume of the system, we envisage our system as representing a fluid flow path, which can be imagined as a column reactor of some total volume (V_T; m^3). The fluid volume (V_f; L) within this reactor is equal to:

$$V_f = V_T \cdot \phi \cdot f_w \cdot 1000 \tag{12}$$

where ϕ is the porosity, f_w is the time- and space-averaged fraction of the total porosity that is fluid saturated, and the factor of 1000 converts from m^3 to liters. The surface area of feldspar in the column (SA$_f$; m^2) is equal to:

$$SA = V_T \cdot (1 - \phi) \cdot f_m \cdot \rho_{mineral} \cdot SSA \cdot f_r \tag{13}$$

where f_m is the volume fraction of feldspar in the solid phase, $\rho_{mineral}$ is the mineral density (g/m^3), SSA is the mineral specific surface area (m^2/g), and f_r is the fraction of the total surface are that is "reactive". We assume no changes in mass, surface area, or porosity occur over the duration of our model simulations. The ratio of fluid volume to feldspar surface area, which we term the water/rock ratio (W/R; L/m^2) is thus equal to:

$$W/R = \frac{\phi \cdot f_v \cdot 1000}{(1 - \phi) \cdot f_m \cdot \rho_{mineral} \cdot SSA \cdot f_r} \tag{14}$$

5. Reaction Equations

The formulations and assumptions described above can be used to formulate a set of equations that describe the time-evolution of Na, Ca, Si, and Al concentrations in a batch reactor undergoing the simultaneous dissolution of anorthite and albite as well as the

precipitation of kaolinite/halloysite:

$$V_f \frac{d[Na]}{dt} = x_s \cdot SA_f \cdot \frac{k_{alb}}{3} \cdot f(\Delta G_{r,alb}) \cdot \mathbf{H}(-\Delta G_{r,alb}) \tag{15}$$

$$V_f \frac{d[Ca]}{dt} = (1 - x_s) \cdot SA_f \cdot \frac{k_{an}}{2} \cdot f(\Delta G_{r,an}) \cdot \mathbf{H}(-\Delta G_{r,an}) \tag{16}$$

$$V_f \frac{d[Si]}{dt} = \left(3 \cdot \frac{d[Na]}{dt}\right) + \left(2 \cdot \frac{d[Ca]}{dt}\right) - \left(2 \cdot SA_k \cdot k_p \cdot \frac{\Delta G_{r,kao}}{RT} \cdot \mathbf{H}(\Delta G_{r,kao})\right) \tag{17}$$

$$V_f \frac{d[Al]}{dt} = \left(3 \cdot \frac{d[Na]}{dt}\right) + \frac{d[Ca]}{dt} - \left(2 \cdot SA_k \cdot k_p \cdot \frac{\Delta G_{r,kao}}{RT} \cdot \mathbf{H}(\Delta G_{r,kao})\right) \tag{18}$$

where $f(\Delta G)$ can either take the form of

$$f(\Delta G) = 1 - \exp\left(\frac{\Delta G}{\sigma RT}\right) \tag{19}$$

or

$$f(\Delta G) = \frac{\Delta G}{\sigma RT} \tag{20}$$

x_s is the fraction of feldpsar surface area contributed by albite, and $\mathbf{H}$(x) is the Heaviside function. For plagioclase dissolution, we use only the TST form of $f(\Delta G)$ (Equation 19). For kaolinite/halloysite precipitation, we test both function forms of $f(\Delta G)$. As our model does not track changing mineral surface areas, it is necessary to include the Heaviside function in order to force kaolinite to only precipitate and feldspar to only dissolve in the model simulations.

6. Model Parameterization

The values of all parameters used in the multi-component batch model are provided in Table S3. For all simulations, we use a temperature of 25°C and initial concentrations of Na, Ca, and Si of 1μM and an initial concentration of Al of 1 pM. We do not adjust the experimental dissolution rate data, which was collected at 22°C, for the slightly elevated temperature. Values for pCO_2, W/R, and initial secondary mineral abundances are varied

between simulations (see Table S3). The thermodynamic data used in our model was taken from Drever et al. (1988).

As stated previously, we use data from Gudbrandsson et al. (2014) to calibrate far-from-equilibrium plagioclase dissolution rates and, near-equilibrium, assume TST behavior. Given the order of magnitude scatter in the experimental rate data (Figure S9) and the well-known lab-field discrepancy in apparent reaction rates (White & Brantley, 2003), we compare both the best-fit rate law and a "slow" rate law that better describes the relationship between the minimum dissolution rates and pH. For precipitation rates, we use a linear fit to the data from Yang and Steefel (2008) to determine the precipitation rate constant (k_p). When applying the TST form of the $f(\Delta G)$ function for precipitation rates, we decrease the value of k_p by a factor of 10.

Some previous work (Maher, 2011) has considered the clay mineral halloysite to be the main control on equilibrium Si concentrations in natural waters. This mineral phase has an identical chemical formula to kaolinite, but it is more soluble than kaolinite. As a test, we compare model simulations using the ΔG_r^0 for either kaolinite or halloysite while otherwise assuming identical kinetic parameters for the two minerals.

To parameterize W/R it is possible to use measurements of mineral surface area and porosity in natural silicate materials or simply to chose a value that generates realistic concentrations over the expected timescales of water-rock reactions in small watersheds (i.e., approximately annual timescales). Realistic values for ϕ, f_m, and SSA are on the order of 10's of percent, 1 to 10 percent, and ~ 0.1 m^2 g^{-1}, respectively. These values predict W/R values between 10^{-2} and 10^{-1} L/m^2. Slightly higher or lower values can be generated by assuming that the fraction of surface are that is reactive (f_r) or the fraction

of pores that are un-saturated (f_w) deviate from 1. Here, we test W/R values between 0.05 and 0.9 , which are consistent with the physical properties of natural weathering systems and capable of generating realistic solute concentrations (i.e., 100's of μM) within 2 years of reaction.

7. Model Results

The multi-component batch model can produce a variety of concentration versus time relationships for cations and Si (Figures S10- S13) including some with an Si overshoot. It is beyond the scope of this work to exhaustively explore the full range of model behavior. Instead, we present a few representative examples that how both structural uncertainty and parameter uncertainty influence the results. It is important to note that our exploration of structural uncertainty is likely too conservative as we do not consider as wide of a range of functional relationships between ΔG_r and reaction rates as has been suggested for silicate systems (Maher et al., 2009; Perez-Fodich & Derry, 2020).

When the concentrations of Al are modeled using Equation 3 (free Al experiments), the calculated values can be higher than expected for natural rivers (Figure S10c). In our model, the only sink for Al is halloysite/kaolinite precipitation. However, in natural systems, there may be other important Al sinks such as the formation of Al oxide minerals. Instead of incorporating a wider range of Al cycling processes, we instead impose lower Al concentrations on the model to see if a Si overshoot is still generated. Specifically, we either assume constant total Al concentrations (constant Al experiments) or prescribe them to increase linearly with time from a set starting value (1 pM; linear Al experiments). As a proof-of-concept, we use a total Al concentration 2 μM for our Al constant experiments.

In our linear Al experiments, the rate of increase is set so that, after 1 year of reaction, the Al concentration is $\sim 1\mu$M (Figure S11b). As with the Al free experiments, the abundance of Al^{3+} is predicted from Equation 3 using the specified total Al concentration and the model predicted pH value for both the constant and linear Al experiments. With these lower and less-variable Al concentrations, the model is still capable of generating a Si overshoot (Figures S11b, S12b,d, and S13b,d).

In Figures S10 and S11, we test the effect of primary mineral composition by varying the fraction of total mineral surface area that is albite. For the free Al model simulations, lower fractions of albite are necessary to generate a Si overshoot (Figure S10b). The linear Al experiments show less sensitivity to primary mineral composition in terms of their ability to generate and Si overshoot (Figure S11b). Presumably, the effect of primary mineral composition relates to the difference between Si to Al ratio of the dissolving and precipitating phases. For example, combining Equations 1 and 2 shows that no dissolved Si is generated from stoichiometrically coupled anorthite dissolution and kaolinite/halloysite precipitation.

In Figure S12, we test the effect water to rock ratios, pCO_2 values, and dissolution rate constants. For this experiment, we use the linear $f(\Delta G)$ function for precipitation rates, an initial secondary mineral surface area to feldspar surface area of 0.5, the ΔG_r^0 value of halloysite, and assume that albite and anorthite contribute equal surface area ($x_s = 0.5$). The model results show a wide range of behaviors. For the free Al models, simulations using the slow dissolution rate do not produce an Si overshoot. Using the best-fit rate law, the largest Si overshoot is produced using the highest W/R and pCO_2 with the free Al model. The linear Al models tend to produce much higher maximum Si concentrations

relative to the free Al models. Using the best-fit rate law, the largest Si overshoot is produced using the lowest W/R and highest pCO_2 with the linear Al model.

In Figure S13, we test the effect of different clay mineral solubilities, initial clay surface areas, and the form of the ΔG function for clay precipitation. For this experiment, we use a water to rock ratio of 0.4, a pCO_2 of 0.07, the best-fit dissolution rate constants, and a surface area fraction anorthite of 0.5. Similarly shaped Si versus time relationships are produced independent of whether halloysite or kaolinite is assumed to be precipitating. Though, using the higher solubility of halloysite produces higher Si concentrations overall. In the constant Al experiments, increasing the initial surface area of secondary minerals leads to a larger Si overshoot. In the free Al experiments, the middle value for the surface area ratio produces the largest Si overshoot. When using the TST style f(ΔG) function, only the constant Al experiments produce an Si overshoot for the specific range of parameters tested here.

Table S1. 2BK model parameter sets identified by k-means clustering

	η	S_U^*	S_L^*	β_U	β_L
1	0.66	368.25	789.17	14.26	47.10
2	0.41	97.45	2444.43	11.54	32.46
3	0.83	86.82	3546.14	6.36	31.11
4	0.42	65.64	5251.91	13.19	17.07
5	0.64	138.83	895.09	7.12	21.31
6	0.17	189.73	4486.60	11.50	7.23
7	0.07	59.96	1413.48	6.24	22.19
8	0.20	152.97	3578.27	12.36	19.78
9	0.65	366.32	4062.09	4.58	27.71
10	0.73	69.07	3029.45	17.64	22.30
11	0.62	419.32	1005.09	14.81	48.39
12	0.62	56.13	1779.04	13.38	18.42
13	0.68	200.75	746.20	13.02	9.00
14	0.78	91.84	3983.33	9.06	39.26
15	0.79	43.91	5284.61	12.96	22.26
16	0.42	69.47	3722.26	16.86	43.75
17	0.58	229.60	5202.10	4.57	40.30
18	0.68	64.75	1465.23	2.95	4.98
19	0.27	481.48	4238.42	10.27	26.64
20	0.27	105.71	4029.36	10.38	31.45
21	0.34	173.44	7045.78	9.74	24.57
22	0.82	60.57	2383.84	14.28	39.46
23	0.47	124.25	5781.44	13.72	43.29
24	0.76	119.98	1071.74	6.32	22.61
25	0.51	144.54	704.19	2.90	9.81
26	0.64	67.73	3386.81	12.79	30.08
27	0.32	238.87	1098.96	14.05	28.26
28	0.13	177.91	4915.50	9.25	16.74
29	0.10	73.23	1817.96	4.44	17.72
30	0.54	202.88	537.68	18.16	19.66

Table S2. Weathering model parameter sets identified by k-means clustering

model	$[C_+]_{eq}/\chi[Si]_{eq}$	Rp/Rd	m,p	m,d
1	7.41	0.53	1.56	1.33
2	9.44	0.14	1.39	1.58
3	2.16	45.27	1.94	1.45
4	8.06	0.31	1.47	1.84
5	6.16	0.10	1.48	1.26
6	5.92	4.25	1.79	1.32
7	2.68	0.12	1.24	1.44
8	6.44	1.12	1.93	1.36
9	2.08	0.41	1.91	1.57
10	7.65	0.24	1.87	1.15
11	5.12	0.20	1.70	1.54
12	5.73	3.45	1.05	1.76
13	2.58	0.72	1.12	1.47
14	9.57	0.12	1.10	1.24
15	3.59	0.41	1.42	1.52
16	5.59	26.66	1.56	1.29
17	1.16	21.04	1.03	1.43
18	1.48	0.77	1.79	1.68
19	4.53	0.12	1.13	1.56
20	7.48	1.69	1.44	1.78

Table S3. Parameters used in the multi-component batch model

Variable	Symbol	Values
fraction of total surface area that is albite	x_s	range from 0.1 to 0.9
best-fit albite log rate constant (mol Si cm^{-2} s^{-1})	$\log_{10}(k_{alb})$	(0.049 (pH^2)) + (-0.604 pH) - 13.25
slow albite log rate constant (mol Si cm^{-2} s^{-1})	$\log_{10}(k_{alb})$	(0.047 (pH^2)) + (-0.6 pH) - 13.82
best-fit anorthite log rate constant (mol Si cm^{-2} s^{-1})	$\log_{10}(k_{an})$	(0.091 (pH^2)) + (-1.36 pH) - 9.66
slow anorthite log rate constant (mol Si cm^{-2} s^{-1})	$\log_{10}(k_{an})$	(0.09 (pH^2)) + (-1.31 pH) - 10.4
temperature (K)	T	298
albite standard state ΔG_r (kJ/mol)	ΔG_r^0	-11.2
anorthite standard state ΔG_r (kJ/mol)	ΔG_r^0	-137.7
kaolinite (halloysite) standard state ΔG_r (kJ/mol)	ΔG_r^0	-22.63 (-42.83)
kaolinite rate constant (mol mineral m^{-2} sec^{-1})	k_p	2.21×10^{-13} (linear) 2.21×10^{-14} (TST)
ratio of initial clay to feldspar surface area	SA_k / SA_f	0.25 to 3.75
temkin's stoichiometric coefficient	σ	3 (feldspar) 2 (kaolinite/halloysite)
water/rock ratio (L/m^2)	W/R	0.05 to 0.9
$AlOH^{2+}$ disassociation constant	K_1	$10^{-4.987}$
$Al(OH)_2^+$ disassociation constant	K_2	$10^{-10.13}$
$Al(OH)_3$ disassociation constant	K_3	$10^{-16.76}$
$Al(OH)_4^-$ disassociation constant	K_4	$10^{-22.16}$
Henry's law constant	K_H	$10^{-1.47}$
carbonic acid disassociation constant	K_i	$10^{-6.35}$
CO_2 partial pressure (atm)	pCO_2	0.007 to 0.07

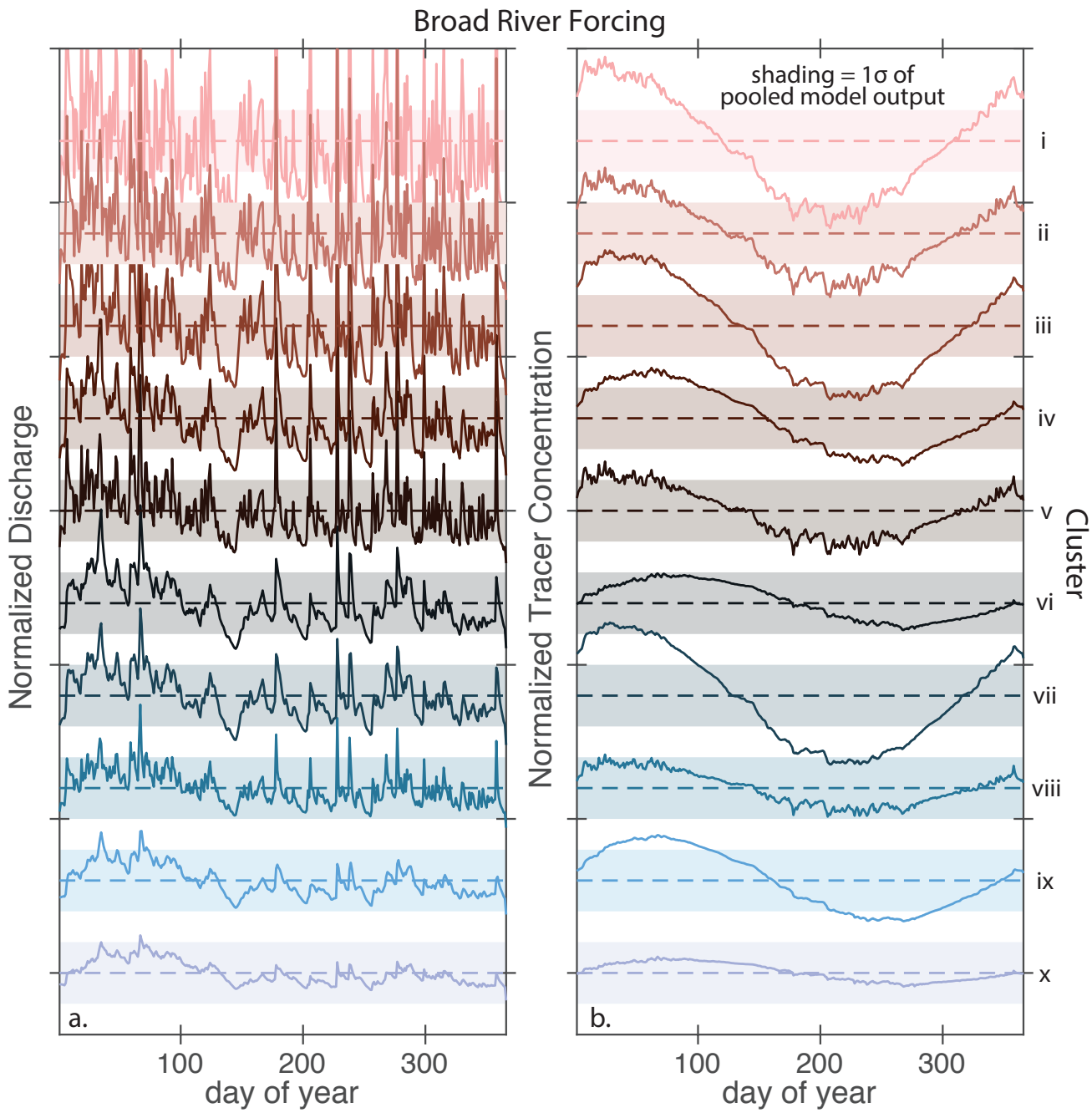

Figure S1. Clustered output from the 2BK model using the Broad River input time-series. (a) The annual cycle of daily average discharge. (b) The annual cycle of daily tracer concentrations. In both panels, the clusters are ordered and color-coded by the standard deviation of the discharge time-series. For each time-series, the dashed line indicates the annual mean for the entire 5000 member ensemble and the shaded band is one standard deviation for the entire 5000 member ensemble.

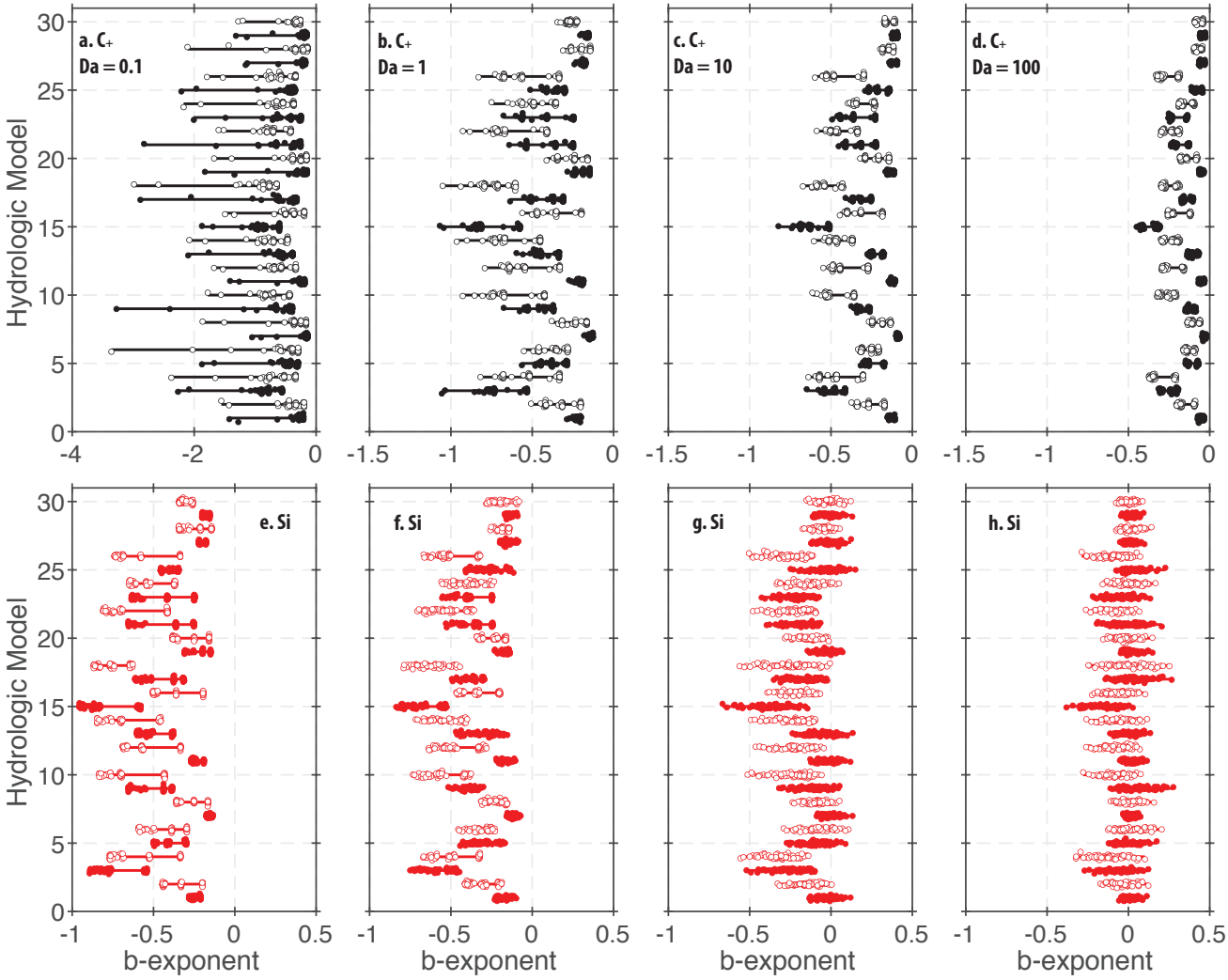

Figure S2. All b-exponents partitioned by 2BK model parameter set (Table **??**).

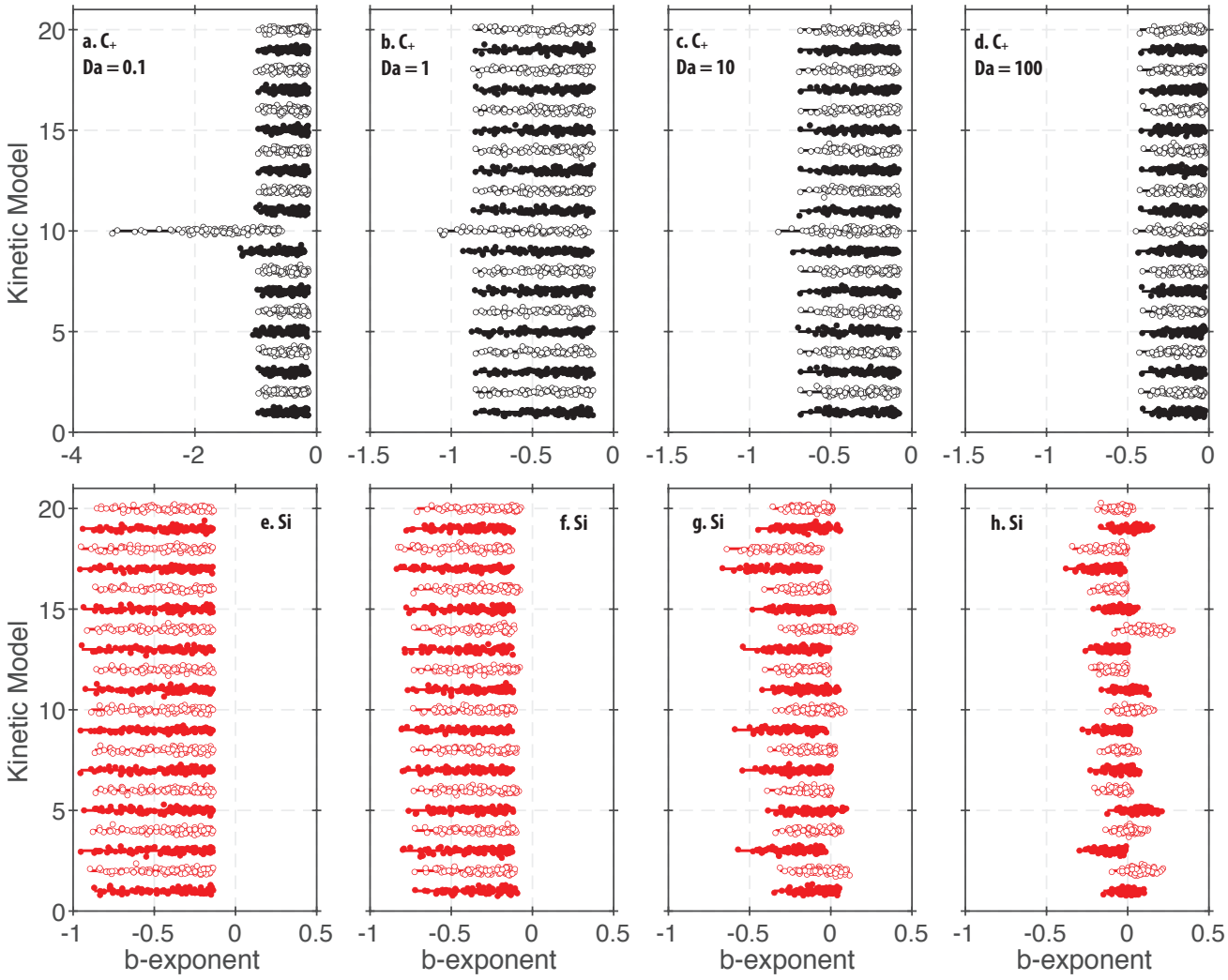

Figure S3. All b-exponents partitioned by weathering model parameter set (Table **??**).

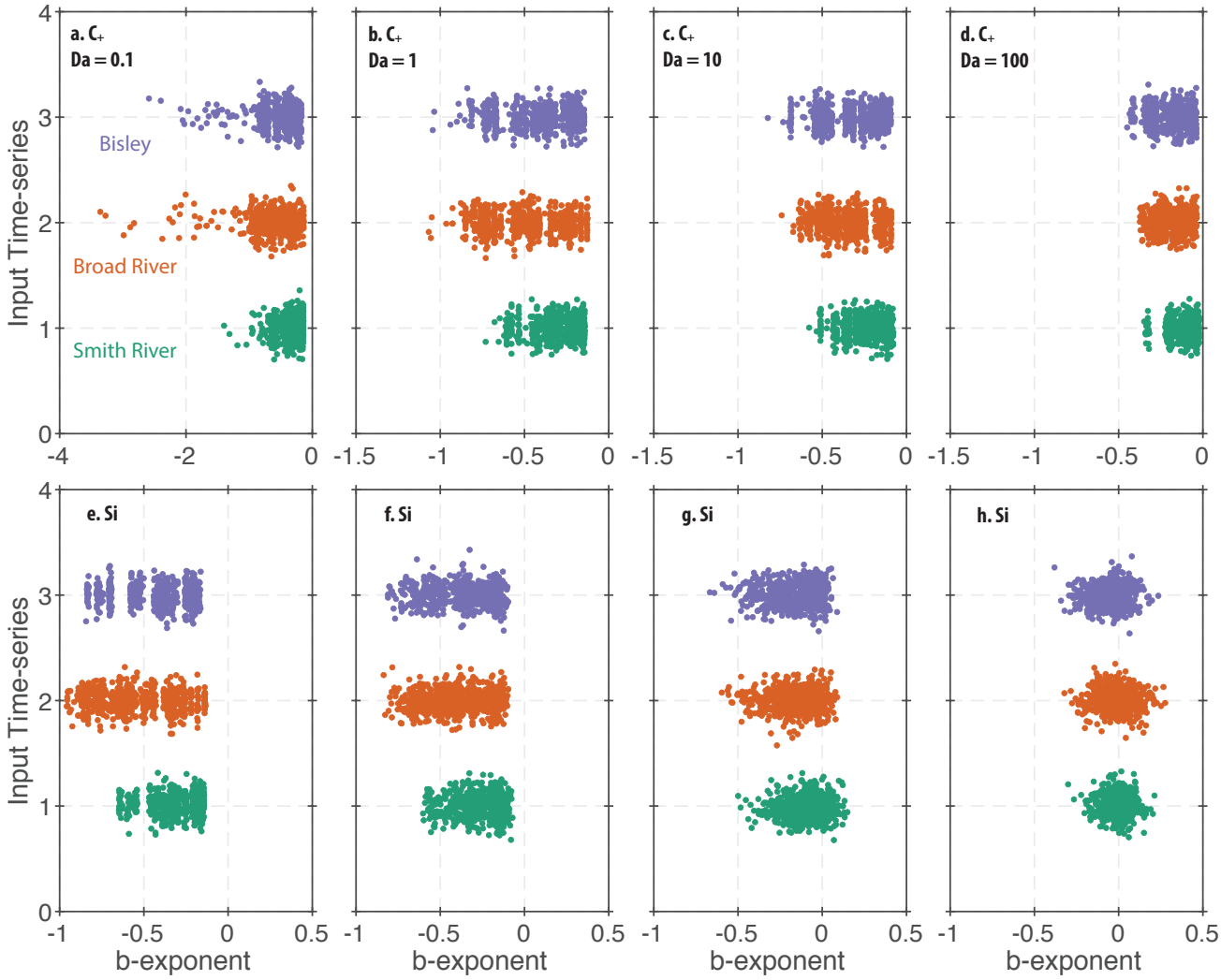

Figure S4. All b-exponents partitioned by input time-series.

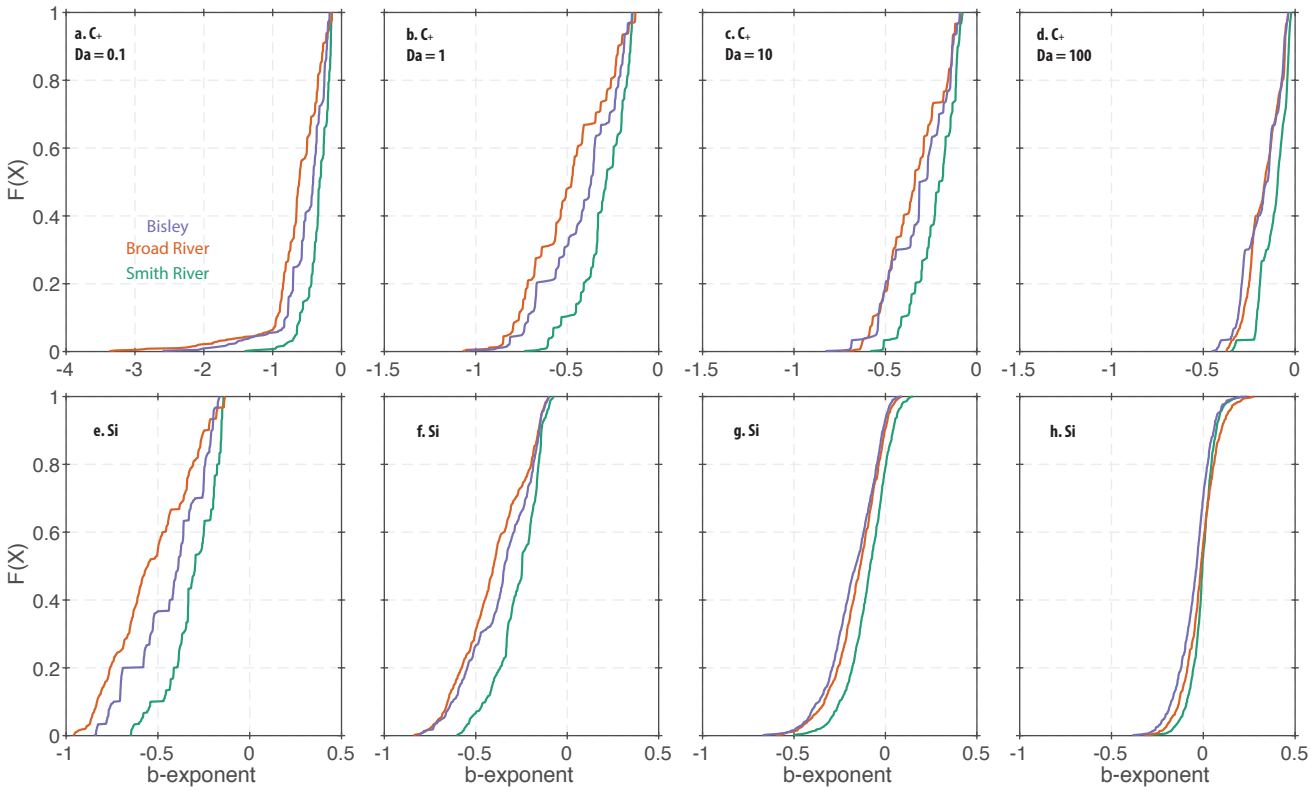

Figure S5. All b-exponents partitioned by input time-series shown as empirical cumulative distribution functions.

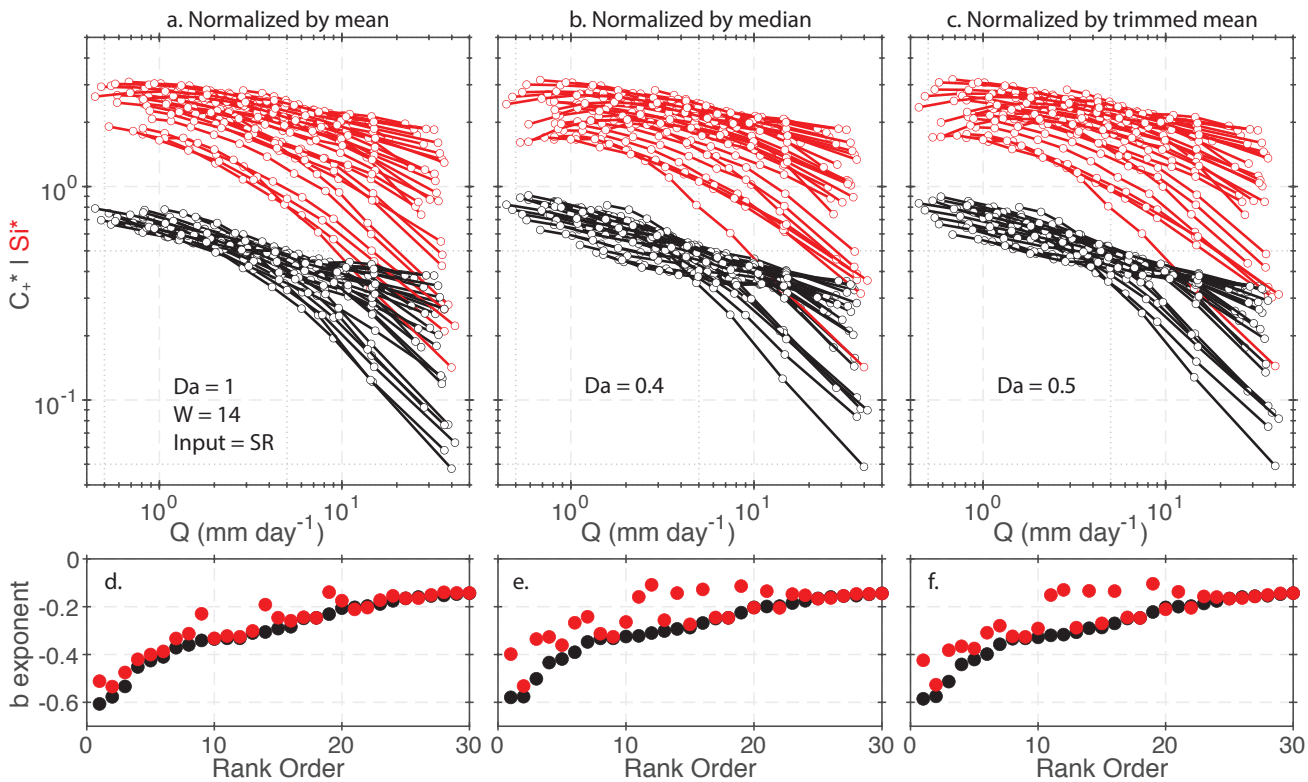

Figure S6. Comparison between different transit time normalization approaches. For each panel, the C-Q relationships were calculated using all 2BK model parameter sets run with the Smith River input forcing and the weathering model parameter set 14. To make a more direct comparison between the different transit time normalization procedures, it is necessary to select different values of Da for each weighting procedure. This is because the proportion of the TTD that is less than T_{eq} will vary at the same Da for the different normalization approaches. So, for panels a-c, which compare normalization by the mean, median, and trimmed mean, respectively, we select Da values of 1, 0.4 and 0.5, respectively. The Da values of 0.4 and 0.5 values are equal to the ratio of the discharge-weighted median to mean transit time and the discharge-weighted trimmed mean to mean transit time, respectively. The three normalization approaches show broadly similar ranges of b exponents, which are shown in panels d-f.

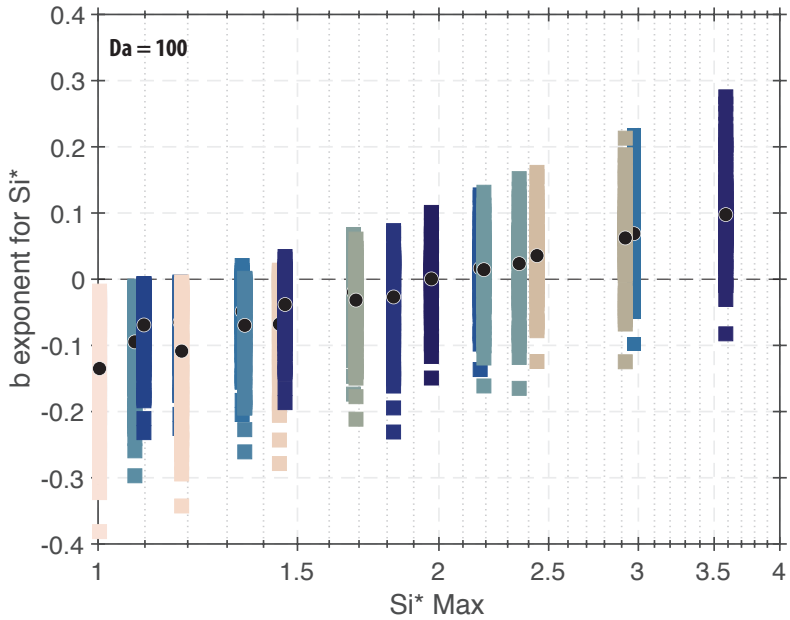

Figure S7. Relationship between the maximum Si* value reached in the dimensionless weathering model and the calculated b exponent for Si* for all of the 90 hydrologic models at a Da value of 100. These results suggest that, in order to produce a positive Si-Q relationship, the maximum Si concentration needs to exceed the equilibrium concentration by 25%. Though, to reach some of the highest b exponents observed in the GloRiCh data, maximum Si concentrations would need to exceed equilibrium concentrations by a factor of 2.

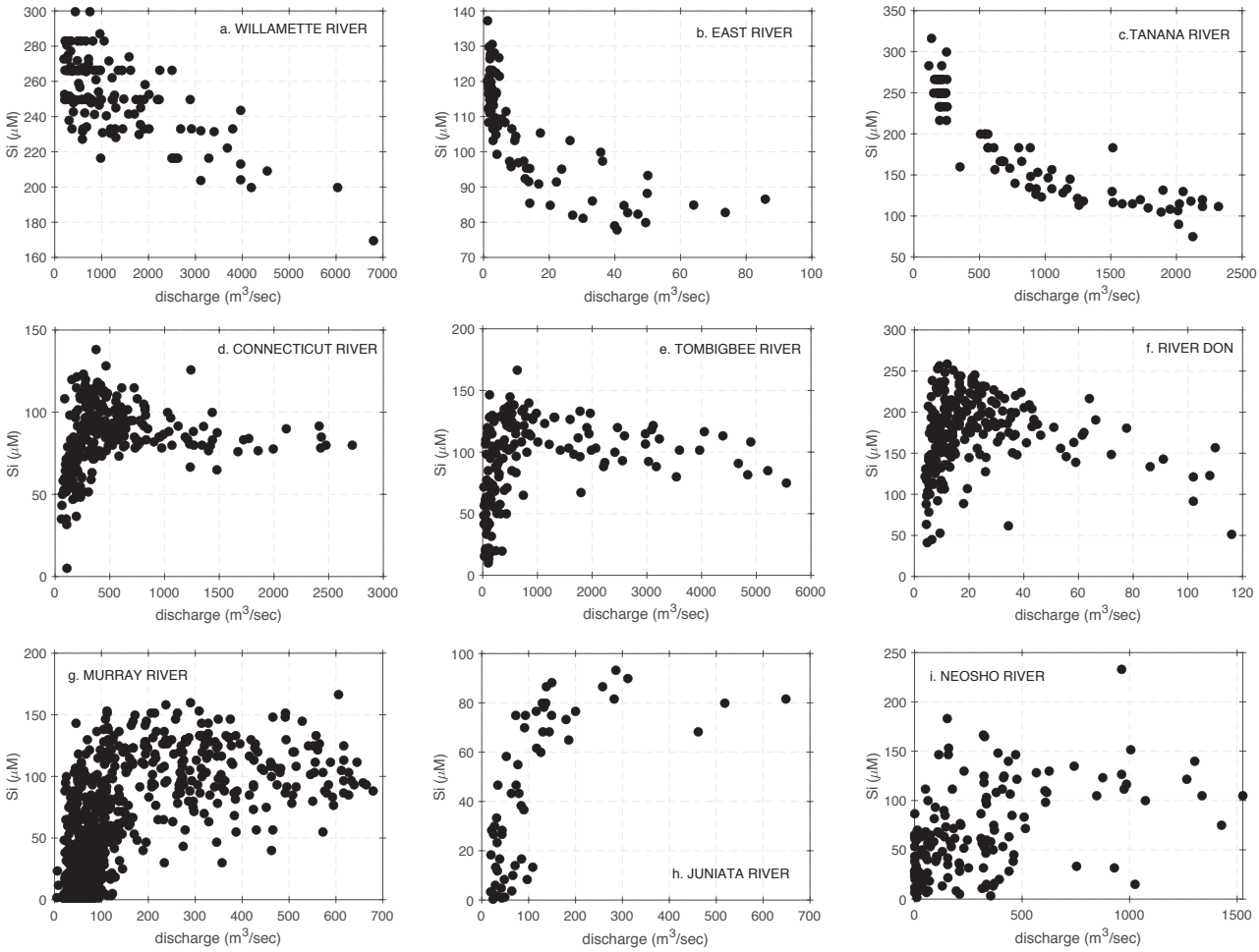

Figure S8. Example silicon-discharge relationships from the GloRiCh database. Panels a-c show example negative Si-Q relationships. Panels d-f show example Si-Q relationships with peaks at intermediate discharge values. Panels g-i show example positive Si-Q relationships.

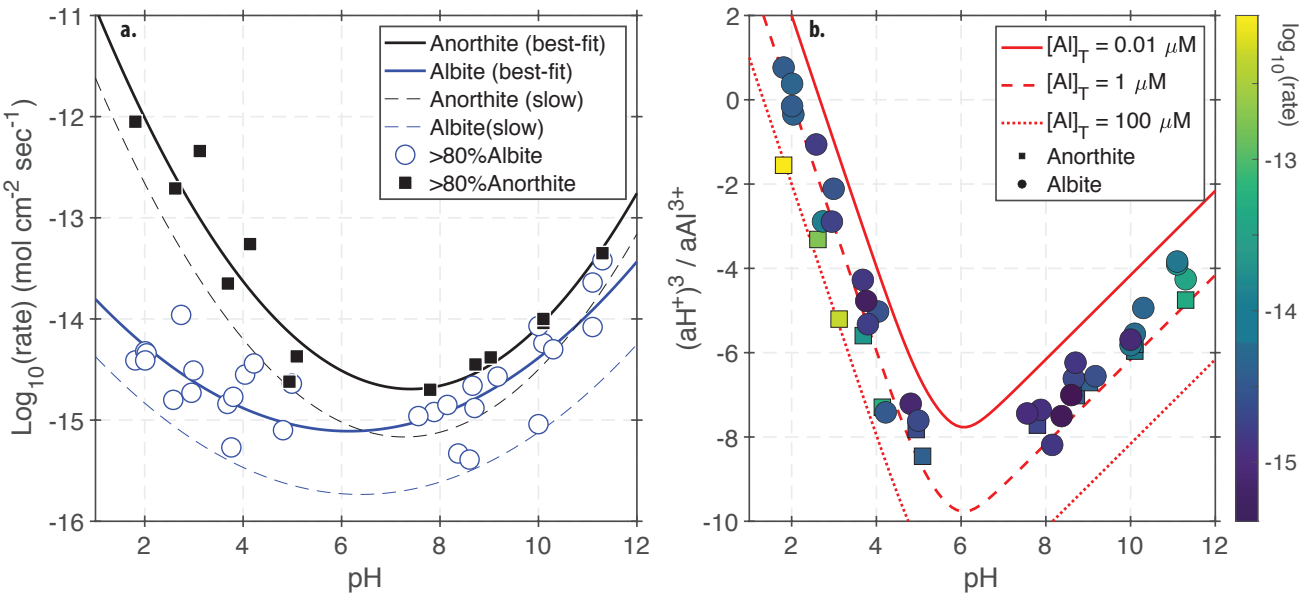

Figure S9. Experimental data from Gudbrandsson et al. (2014) and the effect of Al speciation. (a) Relationship between fluid pH and measured Si release rates. The black squares and blue circles refer to data from experiments where the feldspar composition was greater than 80% anorthite or albite, respectively. The solid and dashed lines show the "best-fit" and "slow" second order polynomials used to parameterize the multi-component model (Table S3). (b) The red lines show the relationship between fluid pH and the ratio of $(H^+)^3$ to Al^{3+} activity predicted by Equation 3 for constant total Al concentrations of 0.01 μM (solid), 1 μM (dashed), and 100 μM (dotted). The symbols show the pH and $(H^+)^3$ to Al^{3+} activity ratios calculated from the Gudbrandsson et al. (2014) data (i.e., the range for which the rate law model is calibrated). As in panel a, squares and circles refer to data from experiments with anorthite and albite. The symbols are color-coded based on the measured dissolution rate (same units as in panel a)

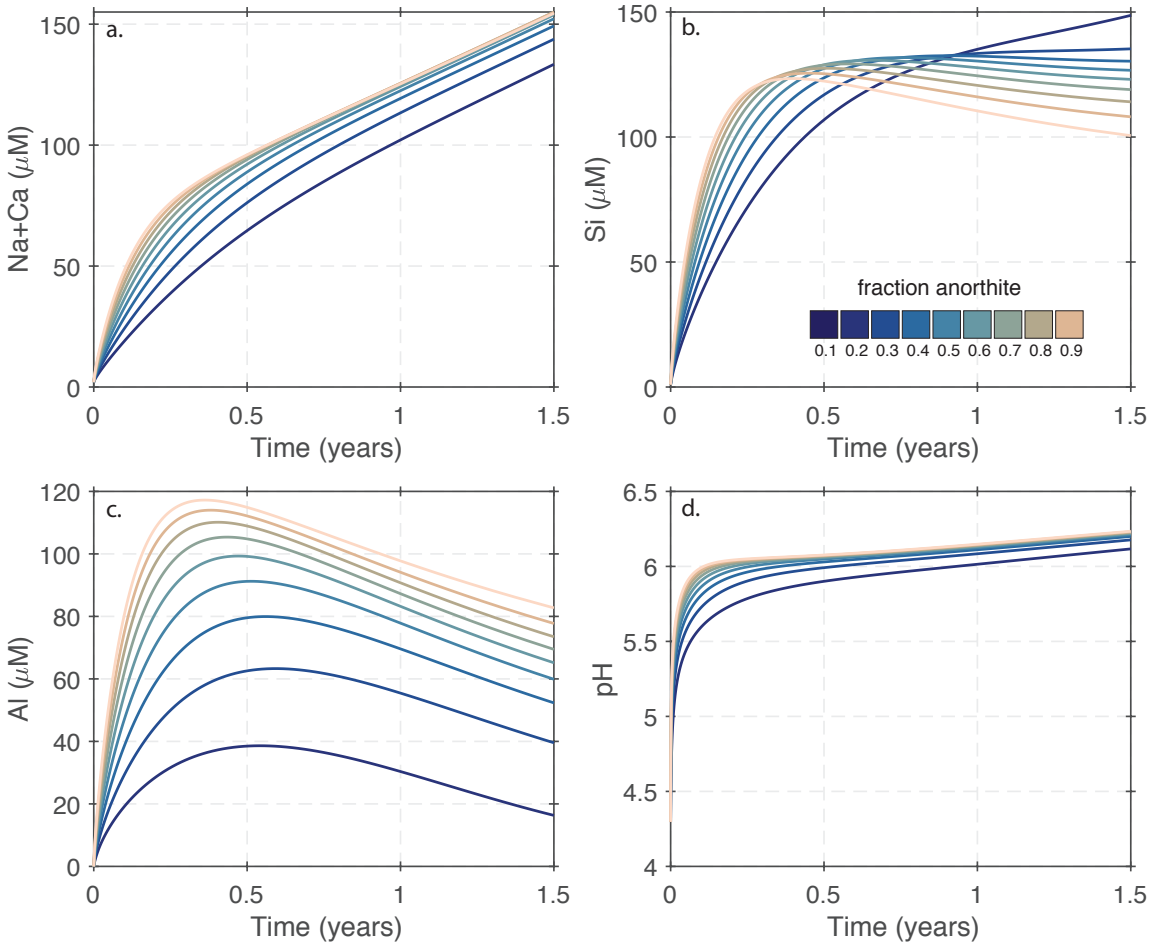

Figure S10. Model predictions of the sum of Na and Ca concentrations (panel a), Si concentrations (panel b), Al concentrations (panel c), and pH (panel d) using the multi-component batch model with the ΔG_r^0 for halloysite, a pCO_2 of 0.01 atm, an initial clay to feldspar surface area ratio of 0.5, and a water-to-rock ratio of 0.9. In each panel, the line color corresponds to the fraction of feldspar surface area contributed by anorthite used in the model simulation.

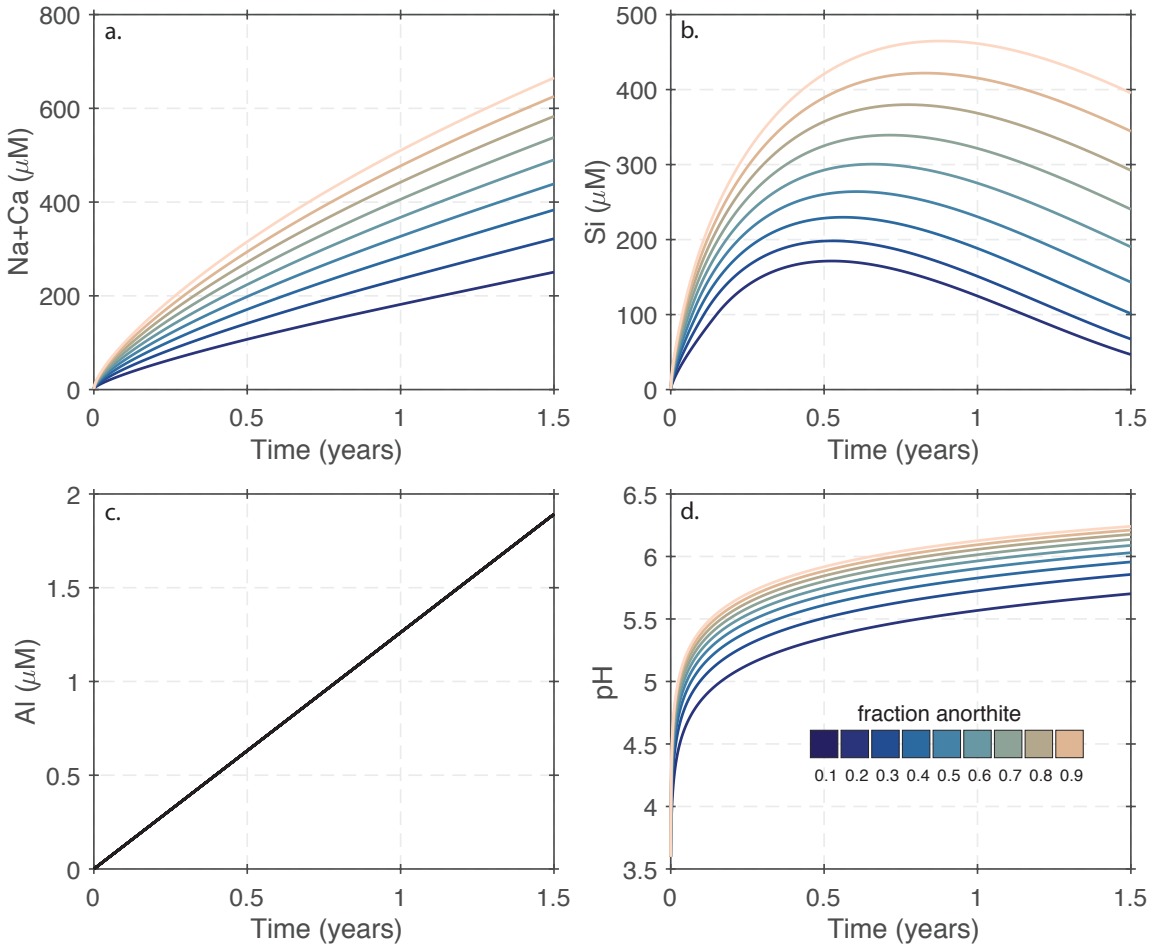

Figure S11. Model predictions using a prescribed linear increase in Al concentrations. Panel a-d show the of the sum of Na and Ca concentrations (predicted), Si concentrations (predicted), Al concentrations (prescribed), and pH (predicted), respectively. The model simulations use the same parameters as used for the output shown in Figure S10, but with the exceptions of a higher pCO_2 (0.05) and higher initial clay to feldspar surface area ratio (3.75). In each panel, the line color corresponds to the fraction of feldspar surface area contributed by anorthite used in the model simulation.

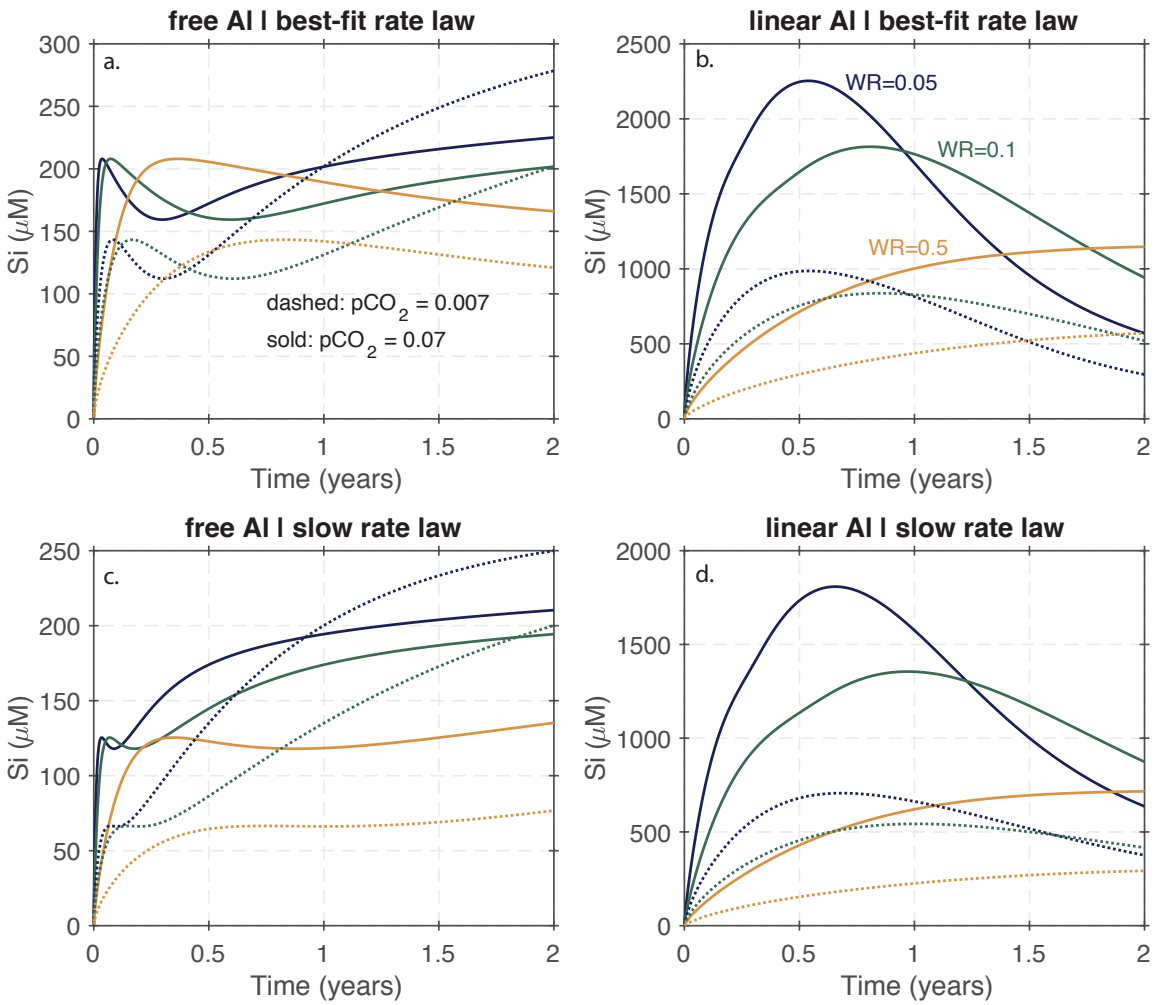

Figure S12. Effect of varying model parameters associated with mineral dissolution on predicted Si versus time relationships. In all panels, the differently colored lines show model simulations with different W/R values of 0.05 (blue), 0.1 (green), and 0.5 (orange). The solid and dashed lines refer to model simulations with pCO_2 values of 0.007 and 0.07 atm, respectively. Panels a and b show simulations using the best-fit rate law whereas panels c and d show simulations using the slow rate law. Panels a and c show simulations where Al concentrations are predicted by the model (free Al) whereas panels b and d show simulations where Al concentrations are prescribed to follow a linear increase (same increase as in Figure S11c). For all of the results shown in all panels, $x_s = 0.5$, $SA_k/SA_f = 0.5$, and the ΔG_r^0 value for halloysite is used.

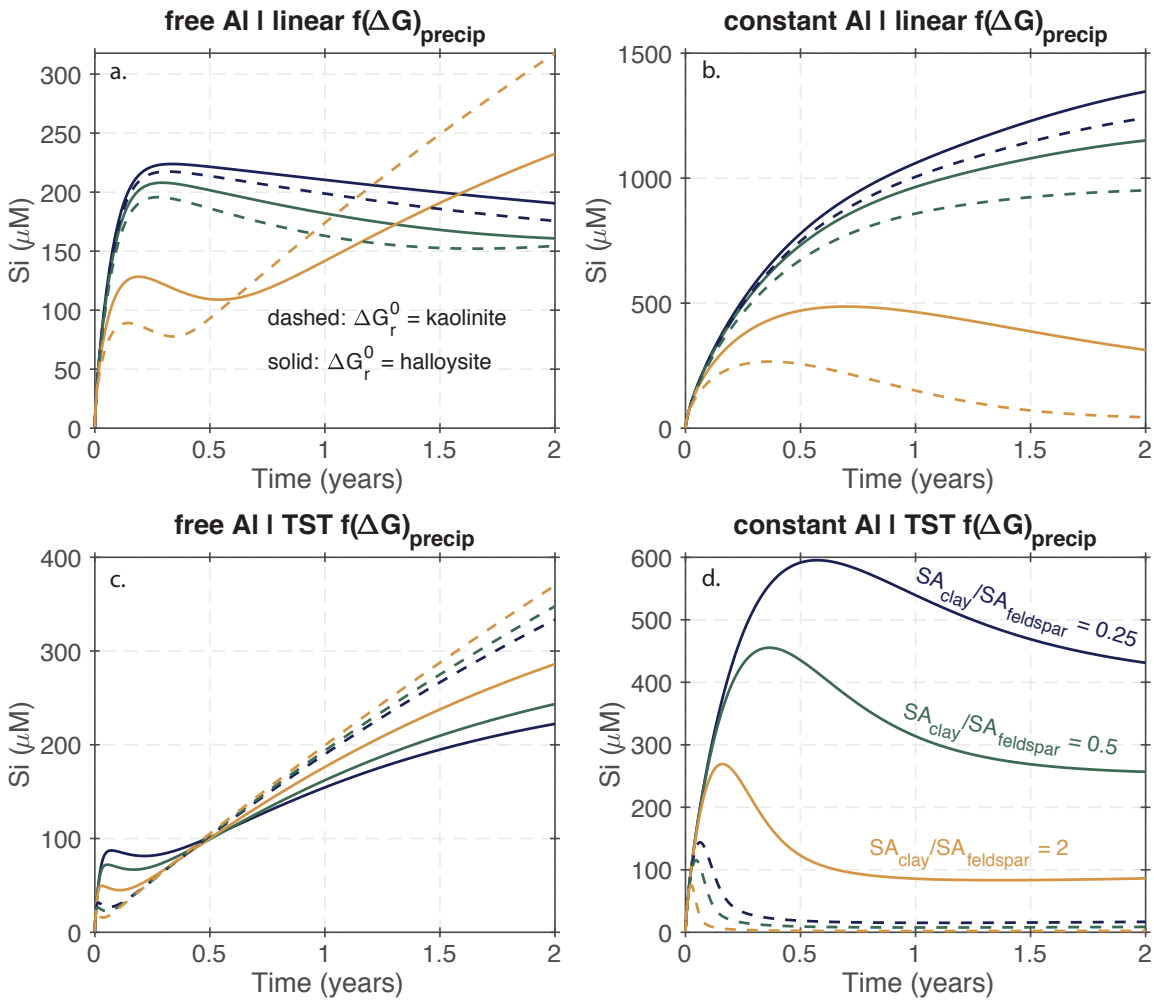

Figure S13. Effect of varying model parameters associated with mineral precipitation on predicted Si versus time relationships. In all panels, the differently colored lines show model simulations with different initial clay to feldspar surface areas of 0.25 (blue), 0.5 (green), and 2 (orange). The solid and dashed lines refer to model simulations using either the ΔG_r^0 value of halloysite or kaolinite, respectively. Panels a and b show simulations using a linear f(ΔG) function whereas panels c and d show simulations using the TST form of the f(ΔG) function. Panels a and c show simulations where Al concentrations are predicted by the model (free Al) whereas panels b and d show simulations where Al concentrations assumed to remain at a constant value of 2 μM. For all of the results shown in all panels, $x_s = 0.5$, $pCO_2 = 0.07$, and W/R = 0.4

References

Arvidson, R. S., & Luttge, A. (2010, January). Mineral dissolution kinetics as a function of distance from equilibrium – New experimental results. *Chemical Geology*, *269*, 79–88.

Drever, J. I., et al. (1988). *The geochemistry of natural waters* (Vol. 437). prentice Hall Englewood Cliffs.

Eiriksdottir, E. S., Gislason, S. R., & Oelkers, E. H. (2013, April). Does temperature or runoff control the feedback between chemical denudation and climate? Insights from NE Iceland. *Geochimica et Cosmochimica Acta*, *107*, 65–81.

Gudbrandsson, S., Wolff-Boenisch, D., Gislason, S. R., & Oelkers, E. H. (2014). Experimental determination of plagioclase dissolution rates as a function of its composition and ph at 22 c. *Geochimica et Cosmochimica Acta*, *139*, 154–172.

Isson, T. T., & Planavsky, N. J. (2018). Reverse weathering as a long-term stabilizer of marine ph and planetary climate. *Nature*, *560*(7719), 471–475.

Maher, K. (2011, December). The role of fluid residence time and topographic scales in determining chemical fluxes from landscapes. *Earth and Planetary Science Letters*, *312*(1-2), 48–58.

Maher, K., Steefel, C. I., White, A. F., & Stonestrom, D. A. (2009, January). The role of reaction affinity and secondary minerals in regulating chemical weathering rates at the Santa Cruz Soil Chronosequence, California. *Geochimica et Cosmochimica Acta*, *73*(10), 2804–2831.

Nagy, K. L., Blum, A. E., & Lasaga, A. C. (1991). Dissolution and Precipitation Kinetics of Kaolinite at 80C and pH 3: The Dependence on Solution Saturation State. *American Journal of Science*, *291*, 649–686.

Perez-Fodich, A., & Derry, L. A. (2020). A model for germanium-silicon equilibrium fractiona-

tion in kaolinite. *Geochimica et Cosmochimica Acta*, *288*, 199–213.

Rimstidt, J. D., Brantley, S. L., & Olsen, A. A. (2012). Systematic review of forsterite dissolution rate data. *Geochimica et Cosmochimica Acta*, *99*(139), 159–178.

Taylor, A. S., Blum, J. D., & Lasaga, A. C. (2000). The dependence of labradorite dissolution and Sr isotope release rates on solution saturation state. *Geochimica et Cosmochimica Acta*, *64*(14), 2389–2400.

Tosca, N. J., Guggenheim, S., & Pufahl, P. K. (2016). An authigenic origin for precambrian greenalite: Implications for iron formation and the chemistry of ancient seawater. *Bulletin*, *128*(3-4), 511–530.

White, a. F., & Brantley, S. L. (2003). The effect of time on the weathering of silicate minerals: why do weathering rates differ in the laboratory and field? *Chemical Geology*, *202*, 479–506.

Yang, L., & Steefel, C. I. (2008). Kaolinite dissolution and precipitation kinetics at 22 c and ph 4. *Geochimica et Cosmochimica Acta*, *72*(1), 99–116.